CENTRO DE INVESTIGACIONES
EN OPTICA, A.C.

“IMAGING SYMMETRIC AND ANTI-SYMMETRIC BEHAVIOR OF OAM-ENTANGLED STATES” – VERSION FINAL. Incluye cambios sugeridos por revisores

Tesis que para obtener el grado de Maestro en Ciencias (Óptica)

Presenta: Juan Nicolás Claro Rodríguez

Director de Tesis: Dr. Roberto Ramírez A.

León · Guanajuato · México
Octubre de 2021

CENTRO DE INVESTIGACIONES
EN OPTICA, A.C.

CENTRO DE INVESTIGACIONES EN ÓPTICA (CIO)

MASTER THESIS

Imaging Symmetric and Anti-symmetric Behavior of OAM-entangled States

Author:
Juan Nicolás CLARO

Supervisor:
Dr Roberto RAMIREZ

A thesis submitted in fulfillment of the requirements for the degree of Maestro en Ciencias - Óptica

October 11, 2021

"*Wisdom comes when it is no longer of any use to us* "

Gabriel García Márquez

CENTRO DE INVESTIGACIONES EN ÓPTICA (CIO)

Abstract

Maestro en Ciencias - Óptica

Imaging Symmetric and Anti-symmetric Behavior of OAM-entangled States

by Juan Nicolás CLARO

Orbital Angular Momentum (OAM) is a degree of freedom of photons promising for a wide variety of high-dimensional quantum applications. These states, as any used in future quantum technologies, need to be manipulated and studied for their use. We use a known technique for tuning the symmetry of OAM states using dove prisms and study the properties of their interference in a spatially resolved measurement. We found that fringes produced depend on the type of symmetry of the state, moreover, we recover the original Hong-Ou-Mandel interferometers from these spatially resolved measurements and analyze the consequences of this symmetric/anti-symmetric superposition on the visibility. Furthermore, we propose two applications of these kinds of measurements, one for high-dimensional quantum teleportation and another one to achieve an image enhancement in quantum ghost imaging.

Acknowledgments

My academic path has been supported by so many people and situations that it is difficult to have everyone present here. However, among them my family stands out, both the one who from a distance has given me their support as well as the one who in their presence I have found a home in Mexico. I would like to thank my advisor Roberto Ramirez for making this project possible, as well as my laboratory colleagues Z. I. Borja, P. Yepiz and A. Ávila for their teachings and ideas.

I thank the Mexican government who, through CONACYT, have made possible my stay at the *Centro de Investigaciones en Óptica (CIO)*.

Contents

List of Figures

List of Abbreviations

BS	**B**eam-**S**plitter
DP	**D**ove **P**rism
EPR	**E**instein **P**odolsky **R**osen
GI	**G**host **I**maging
HG	**H**ermite-**G**auss
HOM	**H**ong-**O**u-**M**andel
HWP	**H**alf **W**ave **P**late
IP	**I**mage **P**lane
LG	**L**aguerre-**G**auss
SLM	**S**patial **L**ight **M**odulator
SMF	**S**ingle **M**ode **F**iber
SPAD	**S**ingle **P**hoton **A**valanche **D**etector
SPDC	**S**pontaneous **P**arametric **D**own **C**onversion
OAM	**O**rbital **A**ngular **M**omentum
QTP	**Q**uantum **T**ele**p**ortation

To the family I did not choose, and to the one I did.

Introduction

Since the apparition of quantum physics at the beginning of the last century as the most fundamental theory at that time, great technological and scientific advances have been made to lead to a better understanding and manipulation of nature. Furthermore, there are many questions about the quantum character of the systems that remain unanswered.

Many of the most promising applications of quantum physics rely directly on the apparent paradox presented by Einstein, Podolsky, and Rosen (*1*) (EPR). According to this, quantum mechanics must be non-local to be a complete theory, giving the capacity to systems composed of two (or more) isolated parts to be correlated in a way that would be impossible to describe through classical physics. Around 30 years after, J. Bell formulated a theory, based on locality and realism, that unleashed the inequalities known by his name (*2*). This theory allows us to contrast the results of quantum mechanics with those theories based on the so-called hidden variables (*3*). Different experimental tests have been carried out to confirm or disprove these theories, among them those made by A. Aspect stand out (*4*, *5*) along with those made by B. Hensen *et al*, M. Giustina *et al*, and L. K. Shalm *et al* (*6*–*8*), leaving quantum mechanics as the undisputed winner.

Currently, there are many efforts aimed at the study and application of these quantum phenomena into new technologies (*9*–*12*). Among the most promising applications are Quantum Cryptography, Quantum Communication, Quantum Information, and Quantum Computing, all of these grounded in the concept of Quantum Bit (Qubit) and the phenomenon described by the EPR paradox, also known as Quantum Entanglement. For example, there are many algorithms and protocols based on properties of Qubits such as Quantum Teleportation (QTP) (*13*), Entanglement Swapping (ES) (*14*), Quantum Key Distribution (QKD) (*15*), and Superdense Coding (SC) (*16*).

All these applications require a physical platform in which they can be developed at a relatively low technical complexity, allowing the commercial implementation of quantum computing systems in the future. In this sense, all the previous knowledge and technology based on light manipulation made Quantum Optics be one of the firsts and most considered research areas to carry on this job using the photon as a platform (*17*).

Decades ago, it was demonstrated that paraxial beams known as Laguerre-Gauss (LG) modes have a well-defined Orbital Angular Momentum (OAM) (*18*), which assigns integers multiplies of $\hbar$ in angular momentum per photon to the emission. Since then, it has been shown that different families of solutions to the paraxial wave equation satisfy this same property (*19*).

Notwithstanding that it has been known for decades how to produce OAM-entangled states, it is until now that many implementations have been proposed in terms of the possibilities of quantum applications. For example, these paraxial modes can be used to define a discrete Hilbert space with infinite dimension, allowing the production of high-dimensional entangled states using non-linear processes such as Spontaneous Parametric Down-Conversion (SPDC) (*20*), which is desirable for many of the implementations mentioned before (QTP, ES, QKD, and SC)(*21*, *22*). In this way, the possibility of controlling some properties of these states such as the spiral-bandwidth (*23*, *24*), the density matrix (*25*), or its symmetry (or anti-symmetry) broadens the possible applications of OAM-states.

Concerning this last property, a few years ago a way to engineer these paraxial states was proposed (*26*). This was possible through the usage of dove prisms which introduce a relative phase between the photons and tune the symmetry of the state. This idea of

symmetry-tuning has shown to have the potential to empower the development of high-dimensional quantum gates (*27*, *28*), along with its usage in ghost imaging (*29*), among others.

Despite the potential of the spatial structure of these paraxial modes, there are not many advances in the spatially resolved measurement of the properties of such states. For example, for photons entangled in frequency, the Hong-Ou-Mandel interference shape depends strongly on the properties of the joint spectral amplitude and it is possible to predict some of the interference properties using spectrally resolved measurements (*30*). Then, a lot of information could be hidden into a spatially resolved measurement of the symmetry and interference of an OAM-entangled state. This could be of interest for future applications since it would act as an extension for all current applications of the Hong-Ou-Mandel effect (*31*) which will be reviewed in the first chapter.

In this thesis, we implement a spatially resolved version of the experiment implemented by Zhang *et al* (*26*). We show the capability to obtain the symmetric or anti-symmetric Hong-Ou-Mandel interference pattern directly from these spatially-resolved measurements and propose some possible applications related to Quantum Information and Quantum Imaging.

Chapter 1

Theoretical Framework

1.1 Wave Equation

To study the propagation of light, we recall Maxwell's Equations in free space for the electric field $\tilde{\mathbf{E}}$ and the magnetic field $\tilde{\mathbf{B}}$:

$$\vec{\nabla} \times \tilde{\mathbf{E}} = -\frac{\partial}{\partial t}\tilde{\mathbf{B}}, \tag{1.1}$$

$$\vec{\nabla} \times \tilde{\mathbf{B}} = \frac{1}{c^2}\frac{\partial}{\partial t}\tilde{\mathbf{E}}, \tag{1.2}$$

$$\vec{\nabla} \cdot \tilde{\mathbf{E}} = 0, \tag{1.3}$$

$$\vec{\nabla} \cdot \tilde{\mathbf{B}} = 0. \tag{1.4}$$

By taking the curl of (1.1) and replacing (1.2), it can be shown that the complex field $\tilde{\mathbf{E}}$ satisfies the *wave equation*:

$$\nabla^2\tilde{\mathbf{E}} - \frac{1}{c^2}\frac{\partial^2}{\partial t^2}\tilde{\mathbf{E}} = 0, \tag{1.5}$$

similarly for the field $\tilde{\mathbf{B}}$, one obtains:

$$\nabla^2\tilde{\mathbf{B}} - \frac{1}{c^2}\frac{\partial^2}{\partial t^2}\tilde{\mathbf{B}} = 0. \tag{1.6}$$

1.1.1 Paraxial Helmholtz Equation

We can assume a temporal dependence of the fields, leading to the *ansatz* $\tilde{\mathbf{E}} = \xi_i(\mathbf{r})e^{i\omega t}\hat{e}_i$, which can be replaced in (1.5) to derive the *scalar Helmholtz equation* (*19*) for each of the components:

$$\nabla^2\xi_i(\mathbf{r}) + k^2\xi_i(\mathbf{r}) = 0, \tag{1.7}$$

where k is the wavenumber $k = n\omega/c$ i.e., the magnitude of the wave vector $\vec{k} = k_i\hat{e}_i$. The paraxial approximation allows us to introduce considerations about the nature of the propagation of the light, this is, to assume that the direction of $\vec{k}$ is mostly over the propagation axis $\hat{z}$, such that $k_z \gg k_x, k_y$. Therefore, the following approximation for k_z:

$$k_z \approx k - \frac{k_x^2 + k_y^2}{2k}, \tag{1.8}$$

leads to an expression for $\xi_i(\mathbf{r})$ where the factor $e^{ik_z z}$ can be written explicitly as:

$$\xi_i(\mathbf{r}) = u(\mathbf{r})e^{ik_z z}. \tag{1.9}$$

Replacing (1.9) into (1.7) gives a differential equation for the transverse amplitude distribution $u(\mathbf{r})$:

$$\nabla_t^2 u + \frac{\partial^2}{\partial z^2} u + 2ik\frac{\partial}{\partial z} u = 0, \tag{1.10}$$

where the sub-index t denotes the coordinate system perpendicular to z. As the transverse amplitude distribution is expected to vary very slow compared to the factor $e^{ik_z z}$, the second derivative of u with respect to z can be neglected, showing the *paraxial wave equation* (*32*):

$$\nabla_t^2 u + 2ik\frac{\partial}{\partial z} u = 0. \tag{1.11}$$

1.1.2 Families of Solutions of the Paraxial Helmholtz Equation

There are different solutions to (1.11) depending on which transverse coordinate system is chosen. For example, in Cartesian coordinates (x, y) the solution is given by a family of Hermite polynomials, while in polar coordinates, Laguerre polynomials take this place. In the following, some of these solutions are shown.

Hermite-Gauss modes (HG)

In rectangular coordinates, the solution $u(\mathbf{r})$ can be separated into two parts:

$$u_{nl}^{HG}(\mathbf{r}) = u_n^{HG}(x, z)\, u_l^{HG}(y, z) \tag{1.12}$$

to obtain a solution to (1.11) given by the product of a Gaussian with a Hermite polynomial (*19*):

$$u_n^{HG}(x, z) = \frac{B_n^{HG}}{\sqrt{w(z)}} e^{ik\frac{x^2 z}{2\left(z_R^2+z^2\right)}}\, e^{-\frac{x^2}{w^2(z)}}\, e^{-i\left(n+\frac{1}{2}\right)\psi_g(z)}\, H_n\left(\frac{\sqrt{2}x}{w(z)}\right), \tag{1.13}$$

where $w(z)$ is the beam waist, Z_R is the Rayleigh length, $\psi_g(z)$ is the *Gouy phase*, B_n^{HG} is a normalization constant and H_n is the Hermite polynomial of order n. For future references, some of these quantities are shown in terms of the beam parameters as:

$$\begin{aligned} Z_R = \frac{\pi w_0^2}{\lambda}, \quad \tan\psi_g(z) = \frac{z}{Z_R}, \\ w^2(z) = w_0^2\left[1 + \left(\frac{z}{Z_R}\right)^2\right]. \end{aligned} \tag{1.14}$$

Laguerre-Gauss modes (LG)

On the other hand, when the symmetry of the transverse amplitude is cylindrical, the second-order operator ∇_t^2 must be expressed in polar coordinates (ρ, φ):

$$\nabla_t^2 = \frac{\partial^2}{\partial\rho^2} + \frac{1}{\rho}\frac{\partial}{\partial\rho} + \frac{1}{\rho^2}\frac{\partial^2}{\partial\varphi^2}. \tag{1.15}$$

Following a procedure analogous to the previous one, this leads to a solution for $u(\mathbf{r})$ in the form of a product between a Gaussian and a generalized Laguerre polynomial. This is (*19*):

$$u_{lp}^{LG}(\rho, \varphi, z) = \frac{B_{lp}^{LG}}{\sqrt{w(z)}}\left(\frac{\rho\sqrt{2}}{w(z)}\right)^{|l|} e^{-\frac{\rho^2}{w^2(z)}}\, L_p^{|l|}\left(\frac{2\rho^2}{w^2(z)}\right) e^{-ik\frac{\rho^2 z}{2\left(z_R^2+z^2\right)}}\, e^{-i(2p+|l|+1)\psi_g(z)}\, e^{il\varphi}, \tag{1.16}$$

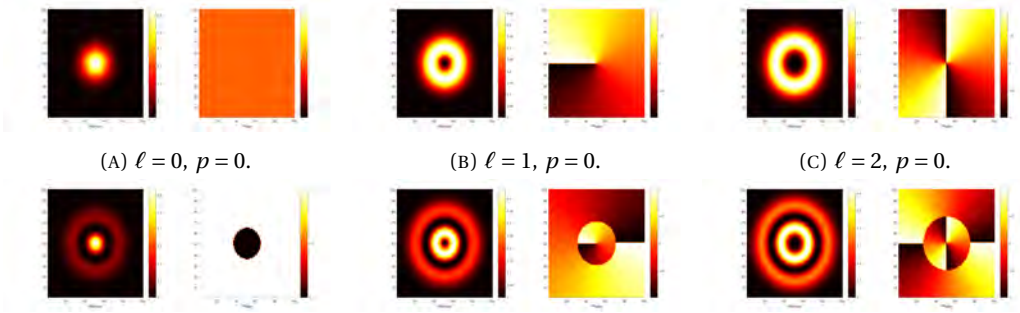

(A) $\ell = 0,\ p = 0.$ (B) $\ell = 1,\ p = 0.$ (C) $\ell = 2,\ p = 0.$

(D) $\ell = 0,\ p = 1.$ (E) $\ell = 1,\ p = 1.$ (F) $\ell = 2,\ p = 1.$

FIGURE 1.1: Transverse intensity distributions and phase fronts produced by beams in LG modes for $\ell = 0, 1, 2,$ and 3 with $p = 0$ and 1.

where l and p are the azimuthal and the radial indexes respectively, and $L_p^{|l|}$ is the generalized Laguerre polynomial. The term $e^{il\varphi}$ is a helical phase that grows with $|l|$ and whose orientation is determined by the sign of this index. Figure 1.1 shows the intensity distributions produced by the first two LG azimuthal modes. This helical phase gives rise to the OAM in this kind of beam mode and is going to be discussed in section 1.1.3.

1.1.3 Orbital Angular Momentum of Paraxial Light Beams

As it was mentioned previously, LG modes carry a well-defined OAM due to the $e^{il\varphi}$ factor, defining an amount of $l\hbar$ units per photon. Due to the properties of LG modes (complete and orthonormal) they can be used to define the basis for describing the OAM state of a single photon. Since all the modes with the same ℓ value have the same OAM, they are degenerated in the p index, leading to what is referred to in the literature as spiral harmonics:

$$C_\ell \left|\ell\right\rangle = \sum_p C_{p,\ell} \left|p, \ell\right\rangle, \tag{1.17}$$

so that the state of the photon in the OAM basis is expressed as:

$$\left|\psi\right\rangle = \sum_\ell C_\ell \left|\ell\right\rangle. \tag{1.18}$$

In other words, LG modes can be used to describe the quantum state of a single photon in the OAM degree of freedom.

On the other hand, even though HG modes do not have a well-defined helical phase $e^{il\varphi}$, it is possible to find a unitary transformation between them and the LG modes (*33*).

1.2 Quantum Information

In classical information theory, the binary unit or *bit* is the basic unit of information. This represents the logical state of a system such as on/off, true/false, up/down, among others. Quantum information theory is built over a similar concept: the *quantum bit* or *Qubit*. While bits have only two possible values usually represented as 0 and 1, qubits have the property of superposition inherited by the quantum mechanics, allowing them to a full continuous spectrum between the two commonly taken values.

$$\text{bit} \rightarrow 0 \text{ or } 1 \qquad \text{Qubit} \rightarrow \left|\psi\right\rangle = \alpha\left|0\right\rangle + \beta\left|1\right\rangle$$

One important fact that must be pointed out about qubits and is, again, inherited from its quantum behavior: when a qubit is measured, there are only two possible outcomes, 0 and 1 with probabilities $|\alpha|^2$ and $|\beta|^2$ respectively. This means that quantum properties of qubits are available only before a measurement is performed, afterwards, they behave as classical bits.

In principle, any quantum system limited to two states can be considered as a platform for the physical realization of qubits. For example, the polarization of photons (*34*), electron's spin (*35*), and cold atoms (*36*) with two levels are some of the commonly used platforms for applications nowadays.

The concept of qubit can be generalized to higher-dimensional quantum systems, known as *qudits*, which can have any number of discrete levels. This generalization leads to a greater number of possibilities about what can or cannot be done with qubits. For example, qudits carry a larger amount of information than qubits, have a lower cloning fidelity, and lead to stronger violations of Bell's inequalities (*20*)

$$\text{Qdits} \rightarrow \left|\psi\right\rangle = \sum_{i=0}^{d} a_i \left|i\right\rangle .$$

In this sense, OAM modes can be used as a platform to study qudits since they belong to a high-dimensional Hilbert space as equation (1.18) shows, depending on how many ℓ indices are taken. This allows the usage of OAM entangled states for all quantum high-dimensional applications and is the reason why its study is of interest (*20*, *37*, *38*). Moreover, OAM modes contain rich properties derived from their spatial structure and the study of these properties might allow new theoretical research and novel applications.

1.2.1 Bell States and Superdense Coding

Consider a two qubit system, A and B, which states are given by the general form:

$$\left|\psi\right\rangle_A = \alpha\left|0\right\rangle_A + \beta\left|1\right\rangle_A \qquad \left|\phi\right\rangle_B = \gamma\left|0\right\rangle_B + \delta\left|1\right\rangle_B , \tag{1.19}$$

such that the joint state $|\Psi\rangle$ might be expressed as:

$$\begin{aligned} |\Psi\rangle_{AB} &= \left|\psi\right\rangle_A \left|\phi\right\rangle_B \\ &= \alpha\gamma\left|00\right\rangle_{AB} + \alpha\delta\left|01\right\rangle_{AB} + \beta\gamma\left|10\right\rangle_{AB} + \beta\delta\left|11\right\rangle_{AB} . \end{aligned}$$

This result suggests that a change of basis can be done between the computational basis $\{|00\rangle, |01\rangle, |10\rangle, |11\rangle\}_{AB}$ and any other as long as dimension is preserved. Among all possible choices, the Bell-states basis (or just Bell basis) is a usual candidate that has many properties and advantages for the description of certain (entangled) systems. These states are:

$$\begin{aligned} \left|\Psi^{\pm}\right\rangle_{AB} &= \frac{1}{\sqrt{2}}\left(\left|01\right\rangle_{AB} \pm \left|10\right\rangle_{AB}\right) \\ \left|\Phi^{\pm}\right\rangle_{AB} &= \frac{1}{\sqrt{2}}\left(\left|00\right\rangle_{AB} \pm \left|11\right\rangle_{AB}\right) \end{aligned} \tag{1.20}$$

and they represent four maximally entangled two-qubit states and a complete basis for the two qubits system. An important fact about Bell-states is that three of them are symmetric under particle exchange, while $|\Psi^-\rangle$ is anti-symmetric. The transformation between Bell

basis and computational basis is defined by:

$$\begin{aligned} |00\rangle_{AB} &= \frac{1}{\sqrt{2}}\left(\left|\Phi^+\right\rangle_{AB} + |\Phi^-\rangle_{AB}\right) \quad |01\rangle_{AB} = \frac{1}{\sqrt{2}}\left(\left|\Psi^+\right\rangle_{AB} + |\Psi^-\rangle_{AB}\right) \\ |11\rangle_{AB} &= \frac{1}{\sqrt{2}}\left(\left|\Phi^+\right\rangle_{AB} - |\Phi^-\rangle_{AB}\right) \quad |10\rangle_{AB} = \frac{1}{\sqrt{2}}\left(\left|\Psi^+\right\rangle_{AB} - |\Psi^-\rangle_{AB}\right). \end{aligned} \tag{1.21}$$

It is straightforward to notice, since the dimension of the two-qubits space $d = 4$, that the amount of information contained by the system is $\log_2 d = 2$ bits. This is the underlying concept of *superdense coding*, a technique aimed to send a two-bits message encoded in one qubit, as is explained in the original paper by Bennet and Wiesner (*16*). This protocol allows us to increase the amount of information per photon in a communication channel.

In summary, the procedure is as follows. Suppose Alice (A) and Bob (B) share an EPR pair (an entangled pair of qubits) described by one of the Bell-states mentioned before, and Alice wants to send a message to her partner Bob. As Alice knows some quantum mechanics, she wants to take advantage of the dimensionality of the two-qubits system by sending two classical bits to Bob instead of one. As a previous agreement between the parties, some correspondence rule between Bell-states and the two-bits string is set, for example:

$$\begin{aligned} \left|\Psi^+\right\rangle_{AB} &\to 00 \quad |\Psi^-\rangle_{AB} \to 01 \\ \left|\Phi^+\right\rangle_{AB} &\to 10 \quad |\Phi^-\rangle_{AB} \to 11. \end{aligned} \tag{1.22}$$

Then, by applying unitary transformations over her qubit, Alice can encode a two-bits message in the EPR pair without having to manipulate Bob's qubit. After encoding, Alice shall send her qubit through a quantum channel to Bob for him to measure on the Bell basis. Depending on the outcome, Bob will know which one of the two-bits strings was sent by Alice.

1.2.2 Quantum Entanglement of Orbital Angular Momentum

Consider two photons, A and B, described in their OAM basis:

$$\left|\psi\right\rangle_A = \sum_n A_n |n\rangle_A \quad \text{and} \quad \left|\phi\right\rangle_B = \sum_m B_m |m\rangle_B .$$

Then, the joint state of the system is then described by:

$$\begin{aligned} |\Psi\rangle &= \left|\psi\right\rangle_A \left|\phi\right\rangle_B \\ &= \sum_{nm} A_n B_m |n\rangle_A |m\rangle_B \end{aligned}$$

At this point, no assumption has been made regarding the nature of this state. In 2001, Zeilinger and coworkers showed that OAM is conserved in the SPCD process by pumping a BBO crystal with a pump having different values of ℓ_{pump} (-1, 0, and 1) and measuring the OAM of idler and signal photons (*39*). In consequence, if the photon pair is produced using the SPDC process, the OAM of the system must be conserved $\ell_p = n + m$. This conservation rule implies that all the coefficients $A_n B_m$ must be zero if $\ell_p \neq n+m$, leaving only terms in the form:

$$|\Psi\rangle = \sum_\ell A_\ell B_{\ell_p - \ell} |\ell\rangle_A \left|\ell_p - \ell\right\rangle_B .$$

Since the state must be symmetric under the exchange of photons A and B, the coefficients must satisfy $A_\ell B_{\ell_p-\ell} = A_{\ell_p-\ell} B_\ell = C_{\ell,\ell_p-\ell}$. Then, the previous equation leads to:

$$|\Psi\rangle = \sum_\ell C_{\ell,\ell_p-\ell} |\ell\rangle_A \left|\ell_p - \ell\right\rangle_B, \tag{1.23}$$

where the coefficients $C_{\ell,\ell_p-\ell}$ define the spectrum of ℓ modes generated and the so-called *spiral bandwidth* of the beam. It is well known from the literature (*40*, *41*) and expected from intuition (due to symmetries of the system) that coefficients C_ℓ are symmetric under interchange centered around ℓ_p. In consequence, the previous expansion may be re-written in terms of one of the Bell-states defined previously including the OAM index $\left|\Psi^+_{n,m}\right\rangle_{AB} = \frac{1}{\sqrt{2}}(|n\rangle_A |m\rangle_B + |m\rangle_A |n\rangle_B)$ as:

$$|\Psi\rangle = \sum_{\ell=0} C_{\ell,\ell_p-\ell} \left|\Psi^+_{\ell,\ell_p-\ell}\right\rangle_{AB}, \tag{1.24}$$

this state is usually referred to as the SPDC state. It's important to point out that OAM conservation brings some experimental considerations such as col-linear or nearly col-linear emission of the SPDC due to paraxial approximation.

1.3 OAM State Engineering

To visualize symmetric and antisymmetric interference of OAM states, the first step is to generate them. According to Y. Zhang *et al.*, this can be achieved through a couple of Dove Prisms (DP) with a relative angle between them (*26*).

Consider the SPDC state (1.24) in a pair of indices m, n as the initial state:

$$\left|\Psi^+_{mn}\right\rangle_{AB} = \frac{1}{\sqrt{2}}(|m\rangle_A |n\rangle_B + |n\rangle_A |m\rangle_B).$$

This state can be manipulated to generate symmetric and anti-symmetric contributions depending on the m and n indices and the angle between the DP's since they introduce a complex phase $e^{i2m\phi}$ and $e^{i2n\phi}$:

$$\begin{aligned}
\left|\Psi^+_{mn}\right\rangle \to |\Psi_{mn}\rangle &= \frac{1}{\sqrt{2}}(|m\rangle |n\rangle e^{i2m\phi} + |n\rangle |m\rangle e^{i2n\phi}) \\
&= \frac{e^{i(m+n)\phi}}{\sqrt{2}}\left(|m\rangle |n\rangle e^{i(m-n)\phi} + |n\rangle |m\rangle e^{-i(m-n)\phi}\right) \\
&= e^{i(m+n)\phi}\left(\left|\Psi^+_{mn}\right\rangle \cos((m-n)\phi)\right. \\
&\quad \left. + i\left|\Psi^-_{mn}\right\rangle \sin((m-n)\phi)\right).
\end{aligned} \tag{1.25}$$

The AB subscripts have been omitted. Depending on the OAM indices n and m, the adequate angle ϕ is chosen for the appropriate application (see 4). Since m, n can be replaced following the indices of (1.24), a more general expression would be:

$$\begin{aligned}
\left|\Psi^+_{\ell,\ell_p-\ell}\right\rangle \to \left|\Psi_{\ell,\ell_p-\ell}\right\rangle &= e^{i(\ell_p)\phi}\left(\left|\Psi^+_{\ell,\ell_p-\ell}\right\rangle \cos((2\ell-\ell_p)\phi)\right. && (1.26) \\
&\quad \left. + i\left|\Psi^-_{\ell,\ell_p-\ell}\right\rangle \sin((2\ell-\ell_p)\phi)\right), && (1.27)
\end{aligned}$$

showing a dependence on the desired angle as a function of ℓ_p. This more general expression could be important for new applications that require entanglement between, for example, the base mode with $\ell = 0$ (a Gaussian Beam) and the first spiral harmonic $\ell = 1$.

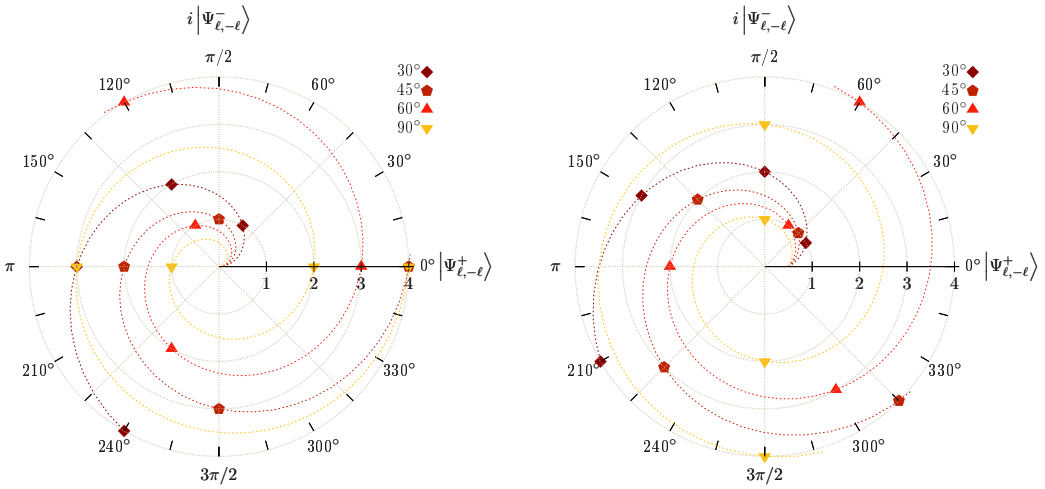

(A) $\ell_p = 0$.

(B) $\ell_p = 1$.

FIGURE 1.2: Symmetry distribution of the different states for a given index ℓ (radial axis) and different values of the angle ϕ between the dove prisms (color key). A dot over the y-axis means that, for that particular ℓ and ϕ, the state is completely antisymmetric; while on the x-axis means that it is symmetric. The index $\ell = 0$ is omitted in both graphs for sake of clarity (since it would be a dot at $r = 0$).

Figure 1.2 shows how the state symmetry depends of the index ℓ and angle ϕ, for different values of the pumping index ℓ_p. For example, if $\phi = 45°$ and $\ell_p = 0$, all even indices $\ell = 2n$ are symmetric while odd indices $\ell = 2n+1$ are antisymmetric. On the other hand, for $\ell_p = 1$ and $\phi = 90°$, there are only antisymmetric contributions for the output state.

1.3.1 HOM Interferometric Filter

Once the desired state is produced, a Hong-Ou-Mandel (HOM) interferometer (*42*) allows us to filter the antisymmetric contribution of a given state (*26*).

The transformations usually used to describe a HOM interference in a 50 : 50 Beam-Splitter (BS) are (*43*):

$$\hat{a}^\dagger \to \frac{1}{\sqrt{2}}(\hat{a}^\dagger + \hat{b}^\dagger)$$
$$\hat{b}^\dagger \to \frac{1}{\sqrt{2}}(\hat{a}^\dagger - \hat{b}^\dagger).$$

We notice that these transformations do not include the ℓ index change over the reflection probability. Since the OAM index is changed under every reflection, the usual HOM transformations must be modified such that this effect is taken into account:

$$\hat{a}^\dagger_\ell \to \frac{1}{\sqrt{2}}(\hat{a}^\dagger_\ell + \hat{b}^\dagger_{-\ell})$$
$$\hat{b}^\dagger_\ell \to \frac{1}{\sqrt{2}}(\hat{a}^\dagger_{-\ell} - \hat{b}^\dagger_\ell),$$

where the sign change under reflections is represented each time a photon changes its original path. With the usual BS transformations, the state $\left|\Psi^-_{\ell,-\ell}\right\rangle$ would be unchanged

after propagation through the BS leading to a coincidence count:

$$\begin{aligned}\hat{U}_{BS}\left|\Psi^{-}_{\ell,-\ell}\right\rangle &= \frac{(\hat{a}^{\dagger}_{\ell}+\hat{b}^{\dagger}_{\ell})(\hat{a}^{\dagger}_{-\ell}-\hat{b}^{\dagger}_{-\ell})-(\hat{a}^{\dagger}_{-\ell}+\hat{b}^{\dagger}_{-\ell})(\hat{a}^{\dagger}_{\ell}-\hat{b}^{\dagger}_{\ell})}{2\sqrt{2}}\left|0\right\rangle_{\ell,-\ell} \\ &= -\frac{\hat{a}^{\dagger}_{\ell}\hat{b}^{\dagger}_{-\ell}-\hat{a}^{\dagger}_{-\ell}\hat{b}^{\dagger}_{\ell}}{\sqrt{2}}\left|0\right\rangle_{\ell,-\ell} = -\left|\Psi^{-}_{\ell,-\ell}\right\rangle. \end{aligned} \tag{1.28}$$

Now, with these modified BS transformations, it is the state $\left|\Phi^{-}_{\ell,-\ell}\right\rangle$ the one that remains unchanged over propagation:

$$\begin{aligned}\hat{U}_{BS}\left|\Phi^{-}_{\ell,-\ell}\right\rangle &= \frac{(\hat{a}^{\dagger}_{\ell}+\hat{b}^{\dagger}_{-\ell})(\hat{a}^{\dagger}_{-\ell}-\hat{b}^{\dagger}_{\ell})-(\hat{a}^{\dagger}_{-\ell}+\hat{b}^{\dagger}_{\ell})(\hat{a}^{\dagger}_{\ell}-\hat{b}^{\dagger}_{-\ell})}{2\sqrt{2}}\left|0\right\rangle_{\ell,-\ell} \\ &= -\frac{\hat{a}^{\dagger}_{\ell}\hat{b}^{\dagger}_{\ell}-\hat{a}^{\dagger}_{-\ell}\hat{b}^{\dagger}_{-\ell}}{\sqrt{2}}\left|0\right\rangle_{\ell,-\ell} = -\left|\Phi^{-}_{\ell,-\ell}\right\rangle. \end{aligned} \tag{1.29}$$

Since $\left|\Phi^{-}_{\ell,-\ell}\right\rangle$ is not an antisymmetric state, it is necessary to map the $\left|\Psi^{-}_{\ell,-\ell}\right\rangle$ state into a $\left|\Phi^{-}_{\ell,-\ell}\right\rangle$ state before propagation through the BS, and back to state $\left|\Psi^{-}_{\ell,-\ell}\right\rangle$ after it, for the interferometer to act as a usual antisymmetric filter. This operation is easily achieved using a couple of mirrors, one before and after the BS, such that reflections are compensated for each path.

In this point, it is important to point out that interference visibility and pattern will depend on the spatial structure of each ℓ mode since we are performing a spatially resolved measurement of this interference.

HOM Interference Dip

In general, the shape of a HOM dip (or peak) will depend on the spectral amplitude functions when the distinguishability of the photons is tuned by a temporal delay. On the other hand, the symmetry of the state will determine if the coincidence probability decrease or increase once the maximum interference is achieved. This effect is observed due to a direct alteration of the photon statistics known as *bunching*, when the two photons take the same output path, or *anti-bunching* in the opposite case (*44*, p. 115). The former is present when the input state is symmetric (like the $\left|\Phi^{+}_{a,b}\right\rangle$, $\left|\Phi^{-}_{a,b}\right\rangle$, and $\left|\Psi^{+}_{a,b}\right\rangle$ states) since the photons leave the BS through the same port; while the latter can be seen as proof of anti-symmetric components of the state (such as $\left|\Psi^{-}_{a,b}\right\rangle$) since the photons leave the BS through different ports.

This could sound contradictory if contrasted with (1.29) since the input state is symmetric but there is a photon on each output. To clarify this apparent contradiction, it is necessary to remember that BS transformations were modified from their original form, that is why the anti-symmetric filter must include a mirror before and after the BS to act as a well-known HOM interferometer.

As an illustrative example, the spectral amplitude function can be modeled as a Gaussian distribution truncated by a $Rect(x)$ since we are using a $\Delta\lambda = 10\ nm$ Band-pass Filter (BPS). The coincidence probability is then obtained as the Fourier transform of the joint spectral amplitude (*43*):

$$
\begin{aligned}
p_c &= \frac{1}{2} \pm \frac{K}{2\pi\sigma^2}\left(\int_{\omega_p/2-\frac{c}{2\Delta\lambda}}^{\omega_p/2+\frac{c}{2\Delta\lambda}} e^{-\left(\frac{\omega-\omega_p/2}{\sigma}\right)^2} e^{-i\omega\tau} d\omega\right)^2 \\
&= \frac{1}{2} \pm \frac{K}{2\pi\sigma^2}\left(\frac{1}{2}\sqrt{\pi}\sigma e^{-\frac{1}{4}\tau(\sigma^2\tau+2i\omega_p)}\left(\Gamma\left(\frac{c}{\Delta\lambda\sigma}+\frac{i\sigma\tau}{2}\right)+\Gamma\left(\frac{c}{\Delta\lambda\sigma}-\frac{i\sigma\tau}{2}\right)\right)\right)^2 \\
&= \frac{1}{2} \pm \frac{K}{2} e^{-\frac{1}{2}(\sigma\tau)^2}\Re\left(\Gamma\left(\frac{c}{\Delta\lambda\sigma}+\frac{i\sigma\tau}{2}\right)\right)^2
\end{aligned} \tag{1.30}
$$

where ω_p is the pumping frequency, σ is the Gaussian width, $\Gamma(z)$ is the complex error function and K is a normalization constant such that the spectral amplitude functions are normalized $\int d\omega|\phi(\omega)|^2 = 1$. The sign $\pm$ is positive if the state is anti-symmetric, and negative if symmetric. Figure 1.3 shows the time delay dependency of the coincidence probability given in equation (1.30). We note that when visualizing HOM interference, symmetric or antisymmetric contributions can be evidenced from the shape obtained as long as photon bunching or anti-bunching is a signature of the symmetry of the state under interference.

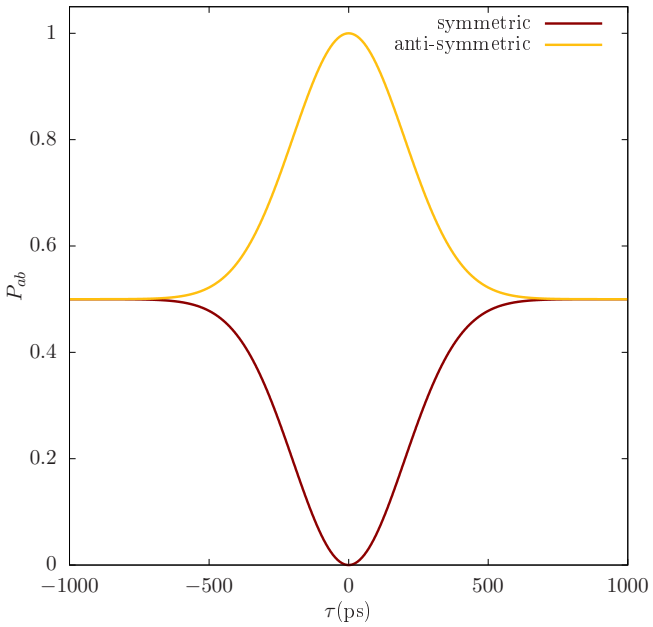

FIGURE 1.3: Coincidence probability plotted against the time delay between the two photons. Here we have taken $\sigma = 0.005\ ps^{-1}$ and $\Delta\lambda = 0.01\ \mu m$

Visibility

From the previous Figure 1.3, a question arises: what happens when the state is neither symmetric nor antisymmetric? From expression (1.25) is clear that there is no restriction about the state symmetry but, instead, a tunable mixture can be achieved through the angle ϕ. The visibility of a HOM interferometer can be defined as (45):

$$
v = \frac{p_c(0) - p_c(\infty)}{p_c(\infty)} \tag{1.31}
$$

where $p_c(0)$ is the coincidence probability at zero path difference $\tau = 0$ and $p_c(\infty) = 0.5$ is the statistical probability of coincidence when $\tau \to \infty$, meaning no interference between the photons. Since the state $\left|\Phi^-_{m,n}\right\rangle$ is the only one leading to coincidence count in equation (1.25) after the BS, a theoretical expression for the maximum reachable visibility is obtained:

$$v = 2\sin^2\left((2\ell - \ell_p)\phi\right) - 1, \tag{1.32}$$

where the sign of v indicates if maximum interference corresponds to a dip (negative) or a peak (positive). If contrasted with Figure 1.2a, this expression clearly shows how the state's symmetry or anti-symmetry influences the maximum visibility that can be achieved. If a state is over the vertical/horizontal axis of this plot, then 100% visibility of the peak/dip should be reachable. On the other hand, if the state is over a diagonal, then it does not have a well-defined symmetry and no peak or dip should be visible, which would be the case of $\phi = \pi/4$ and $\ell_p = 1$.

This expression has to be properly adjusted for experimental testing since, experimentally, perfect visibility $|v| = 1$ is not easy (or even possible) to reach. In fact, this is only an approximation that will allow us to explain some of the obtained results since a real and more accurate expression for v must include a detailed study of the spectral and mode properties from the SPDC source.

In the next chapter, we show our experimental procedure to achieve the objective of visualizing the interference behavior of symmetric and anti-symmetric OAM states, taking into account the concepts embodied in this first chapter.

Chapter 2

Experimental Realization

We based our experimental set-up on the original one made by Yingwen Zhang *et al.* (*26*) which is shown in Figure 2.1, in there a non-collinear SPCD type-I emission is used as OAM entangled states source. Path B contains the pair of Dove prisms (DP) rotated, one respect to the other by $\phi = 45°$, such that the state:

$$\left|\Psi^{+}_{\ell-\ell}\right\rangle \rightarrow \left|\Psi_{mn}\right\rangle \quad = \quad \left|\Psi^{+}_{\ell-\ell}\right\rangle \cos\left(\ell\frac{\pi}{2}\right) + i\left|\Psi^{-}_{\ell-\ell}\right\rangle \sin\left(\ell\frac{\pi}{2}\right), \tag{2.1}$$

is produced, in which, as it was mentioned in the previous section, even elements stay symmetric and odd elements become antisymmetric. The usage of Spatial Light Modula-

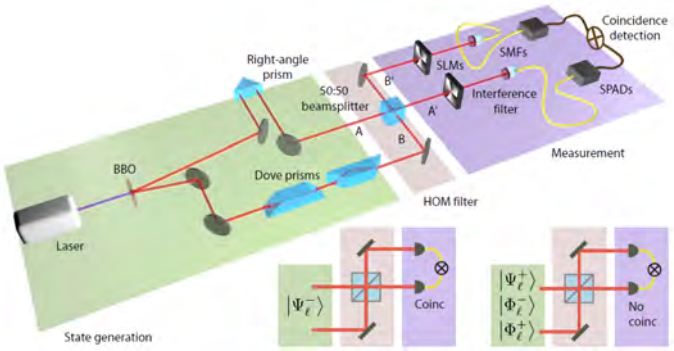

FIGURE 2.1: Original OAM State Engineering set-up, taken from (*26*).

tors (SLMs) allows us, along with a Single-Mode Fiber (SMF) and a Single-Photon Avalanche Detector (SPAD), the experimental implementation of an OAM-state projector depending on what is displayed on the SLM screen (*19*). This mode-projector requires imaging the BBO-crystal plane (intensity and phase) onto the SLM surface to print the corresponding $e^{il\varphi}$ phase into the wavefront. To maximize the collection of light, it is necessary to map this same plane into the $\varnothing \sim 6\mu m$ core of the SMFs. In principle, changing one of the mode-projectors for an iCCD would allow us to visualize the corresponding LG mode along with its interference behavior.

2.1 HOM interferometer

The success of this experiment relies on some key setups. One of these is the HOM interferometer since it acts like an anti-symmetric filter for the joint state and will trigger the image acquisition system.

As a first-step approach, a HOM interferometer (shown in Figure 2.2) was built using a Type-I non-collinear SPDC source. The latter consists of a BBO (Beta barium borate) crystal pumped by a MOGLabs laser at 405 nm wavelength. The wavefront is first coupled to an SMF (405 nm) to filter the laser mode, selecting $\ell_p = 0$ as the OAM pumping index. Then, after a half-wave plate, the laser light is focused on the crystal by a 1000 mm focal distance lens with a beam waist $w_0 \approx 120\mu m$ (see Appendix A).

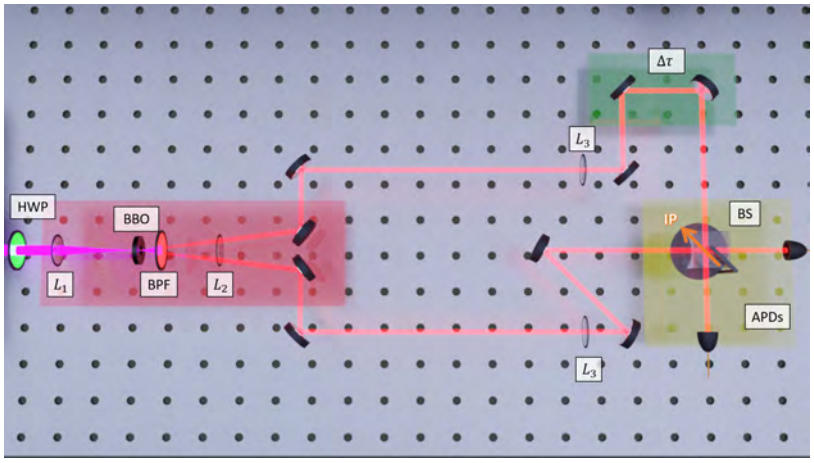

FIGURE 2.2: Experimental implementation of the Hong-Ou-Mandel interferometer. The red zone indicates the photon-pairs source. The green zone contains the temporal delay $\Delta\tau$ and the yellow zone the interference stage, along with the temporal delay and the coupling to the APDs.

A high-pass and a band-pass filter with $\Delta\lambda = 10\ nm$ around 808 nm are added to the SPDC emission to shape the dip/peak width and reach higher visibility. Due to the non-collinear configuration reached by tilting the crystal from its normal incidence, the photon pairs are generated with angles around 1.5 ° from the pumping propagating direction. This latter part is important since OAM conservation demands nearly collinear emission to fulfill the paraxial approximation requirement.

The correlated parts of the cone are overlapped on the semi-reflective face of a 50 : 50 beam-splitter cube by means of a 4f system for each arm, consisting of an $f = 150\ mm$ and two $f = 500\ mm$ lenses. This imaging system allows us to collect more light into the detectors and to interfere the image of the crystal's plane with itself. The time delay is tuned by a two-mirror array disposed over a Newport DC motor with a travel range of 25 mm and a minimum incremental step of 100 nm. The photons coming out from the cube are collected into SMF's by aspheric lenses of 8 mm focal length, leading to single-photon avalanche detectors (SPADs) connected to a NIM Id-800 modulus to register coincidence counts.

It is important to point out that, in this set-up, the OAM index has a passive role since the coupling to the SMFs allows only Gaussian modes ($\ell = 0$) detection. Consequently, the detected photons are indistinguishable on the OAM basis, allowing an almost complete interference.

Once that HOM interference is achieved, DPs are introduced at a relative angle $\phi = 45°$ (as Figure 2.3 shows), such that even OAM-indices stay symmetric and odds become antisymmetric. Due to refraction from DPs glass, an additional delay $\Delta\tau$ has to be added. For N-BK7 glass DPs, the added optical path is around 3 cm for each prism, as our delay is disposed in reflection, the Newport DC motor had to be moved one inch in the optical table. On the other hand, DPs refraction also affects the optical path inside the 4f imaging

system, for which the respective $f = 500\ mm$ lens had to be moved such that the crystal image was mapped again into the BS plane.

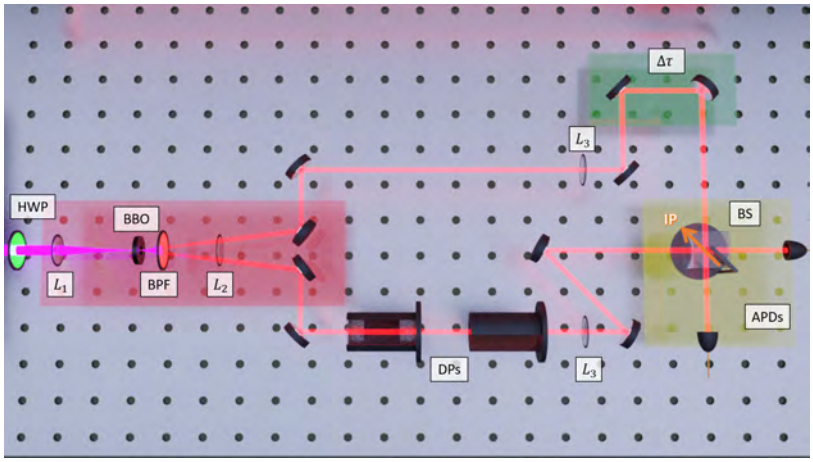

FIGURE 2.3: Addition of the DPs to our Hong Ou Mandel interferometer set-up.

2.2 OAM conservation in Type-I non-collinear SPDC

Once that the interference point was achieved, it was necessary to ensure OAM conservation in this non-collinear arrangement. Based on previous works done in our group (*46*), we used an SLM and an SMF as mode-projector to trigger an iCCD camera disposed after a 28 m-long optical delay. An illustrative scheme is shown in figure 2.4.

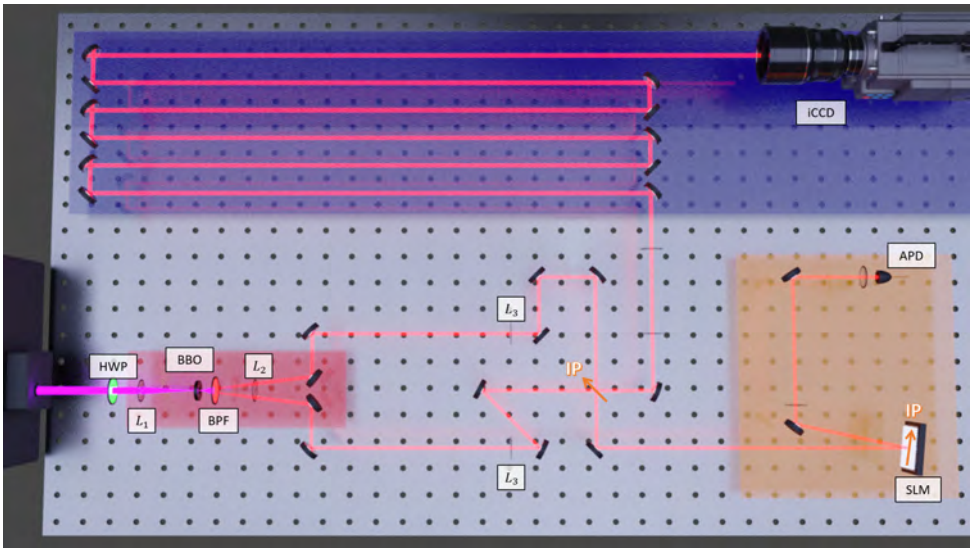

FIGURE 2.4: Set-up employed to visualize the correct OAM conservation in type-I non-collinear SPDC.

To achieve the visualization of this OAM conservation, we removed the BS and the DPs but kept the motor's position. Using a 4f imaging system, the image of the crystal was mapped into a HOLOEYE Pluto SLM from the BS plane. The SLM has a $1920x1080$ display with pixel size $8\mu; m$ and is connected to a computer through an HDMI connection, acting as an extra screen. This SLM reads the green channel from the image displayed and converts it into a phase difference in a non-linear way that has to be characterized to ensure

the correct performance of the device. This characterization was previously done in our group.

To measure a photon with a spiral phase $e^{i\phi\ell}$, it is necessary to transfer an opposite amount of OAM $e^{-i\phi\ell}$ to the wavefront such that it becomes a Gaussian mode, which is able to couple to an SMF. This procedure was achieved by displaying previously-calibrated phase masks into the SLM, known as fork-shaped holograms, which is obtained by the product of the desired vortex term $e^{i\phi\ell}$ with a phase-ramp $e^{iksin(\alpha)x}$. These holograms produce a diffraction pattern similar to a common diffraction grating (see Figure 2.5), but in which each order has an $e^{im\phi\ell}$ phase transferred to it, with m the diffraction order (*47*).

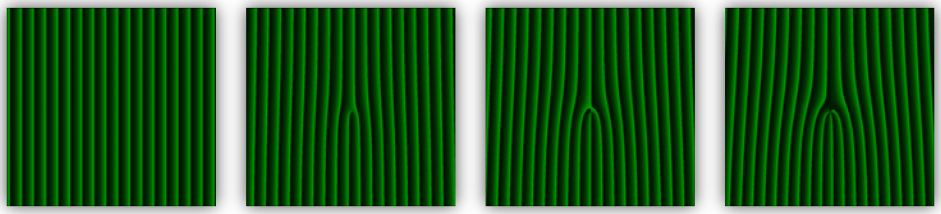

FIGURE 2.5: Fork-shaped holograms projected on the SLM display. From left to right: $\ell = 0, 1, 2, 3$.

In this vein, a fork-shaped hologram was displayed on the SLM screen containing the desired phase dislocation. The first diffraction order was sent through a $x666$ demagnifier image system to be coupled into an SMF and detected by an APD to trigger the iCCD camera, through a NIM modulus, to detect the idler photon.

An additional feature over the usage of SLM has to be discussed in this section. To transfer the desired phase to the wavefront, the difference between a pixel and the other in their green value (the phase difference induced) can not be arbitrarily large, setting a maximum value for the angle α of the phase ramp. This introduces a limitation in the size of the beam w_0, which is why the SPDC mode has to be at least around 800 μm. On the other hand, it is known since the beginning of OAM investigations that a miss-position of the phase mask on the SLM would cause the projection of the mode in a superposition (*39*). This is avoided if the mode is large enough such that the phase mask has some pixels of range to be located properly.

This image acquisition can be done in many planes depending on the image that is sent across the optical delay. For example, adding a lens before the iCCD allow us to vary from a close field from the crystal to a far-field. This will also affect the time necessary to define a properly space-resolved measurement of the LG mode.

2.3 Visualization of symmetric and antisymmetric behavior

Once we ensure the OAM conservation through the mode visualization, the DP's have to be added again along with the BS to re-build the HOM interferometer and the anti-symmetric /symmetric states source. This movement forces us to re-measure the position on the motor such that $\tau = 0$. To be able to change between the imaging system and the interferometer APDs frequently, the two mirrors just after the BS were disposed on flipping mounts as shown in Figure 2.6.

Since the idea is to visualize the symmetric and anti-symmetric behavior of the state (2.1), 71 pictures of 30 s long were taken in a far-field of the SPDC emission each 2 μm beginning 72 μm away from the position for $\tau = 0$. This procedure was repeated for $\ell = 0, 1, 2, 3, 4$.

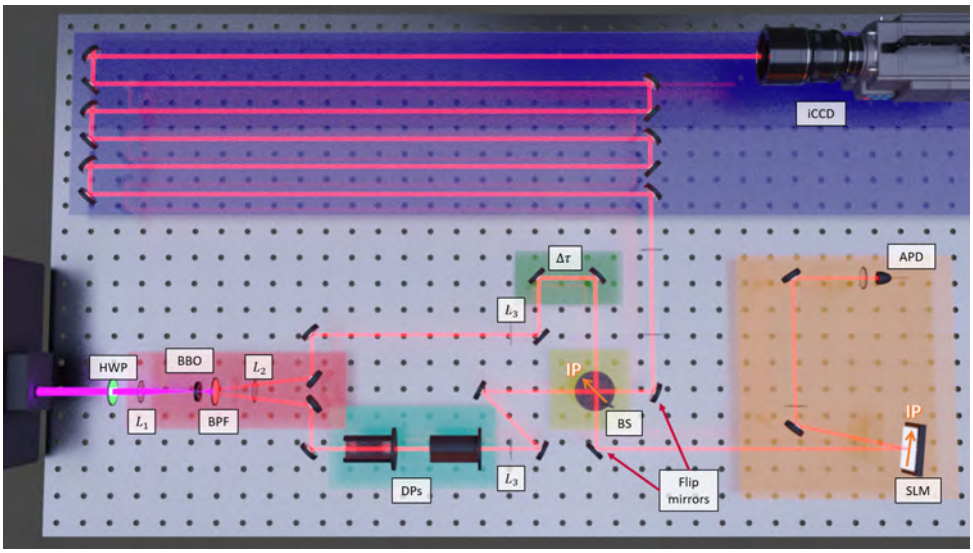

FIGURE 2.6: Symmetric and anti-symmetric behavior visualization setup. The red zone corresponds to an entangled-pairs source, while the cyan zone shows the DPs rotated one from the other to produce the state (1.25). The green zone contains the tunable temporal delay τ and the yellow one corresponds to the BS. The orange zone constitutes the OAM-mode projector to signal the image acquisition (blue zone).

2.4 Alignment

Alignment was done by means of an infrared fiber-laser split in two by a PBS. As a consequence of the non-collinear emission, the reference beams had to be directed at 1.5° and −1.5° from the pump at the crystal's plane. To ensure overlapping of the reference beam and the SPDC emission, close and far-field images were obtained with an Andor iCCD as shown in Figure 2.7.

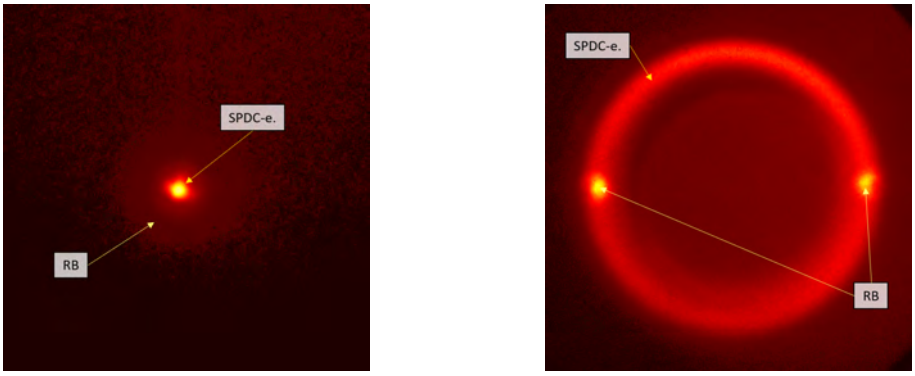

(A) Close-field. (B) Far-field.

FIGURE 2.7: Images of overlapping the reference beam (RB) and the SPDC emission (SPDC-e.) on the (A) close-field and (B) on the far-field. Overlapping on the far-field ensures that the RF and the photons share the same direction.

A 4f imaging system was introduced (not shown on set-up figures) using two removable lenses $f_1 = 125\ mm$ and $f_2 = 300\ mm$ to map the crystal plane into a variable diaphragm. this to preserve the alignment and introduce a pre-magnification of the SPDC emission. This alignment method allowed us to define the image planes (IP) along with a size-controlled

aligning spot, useful when aligning imaging systems such as the demagnifying telescopes and the interference on the BS.

Once that the reference beams transmitted from the BS were coupled to the SMFs (right after the HOM interferometer) a maximum coincidence count of 8000 per second with a 30 mW (measured after the HWP) CW pumping beam was reached just after connecting the fibers to the APDs. We found that any attempt to optimize this coincidence rate with the SMFs coupling leads to a lower number of coincidence counts.

An image of the overlapping of the two correlated zones of the SPDC cone is shown in Figure 2.8. This rotated shape from one of the arms is an additional difficulty since it is not clear which two parts of the cones are anti-correlated in the OAM index. On the other hand, the two parts of the cone have to travel as collinear as possible after the interference, such that both have the same phase transference on the SLM plane and can be collected by the SMF; at the same time, these anti-correlated zones must overlap on the image captured by the iCCD. Regarding this last part, it is worth mentioning that high visibility depends (experimentally speaking) on how well the modes are overlapped on the BS and, if they do not travel in a collinear way after interfering, interference fringes will appear in the image taken in coincidences.

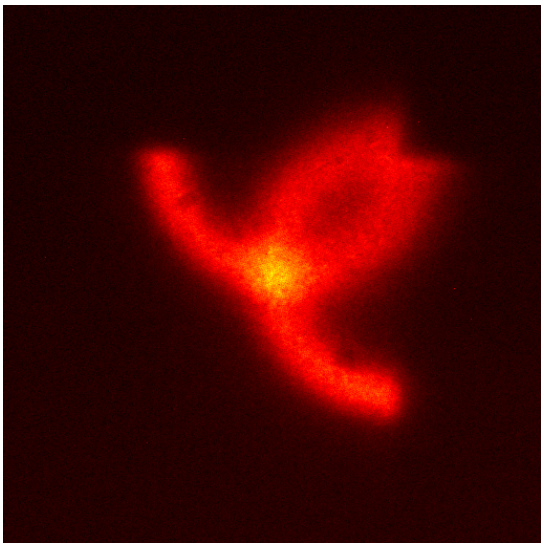

FIGURE 2.8: When overlapped, the two diametrically opposite zones of the SPDC cone draw a cross-shaped image since one of the arms is rotated by the DPs. This is an additional difficulty to the experiment since it is not easy to find the exactly two correlated zones to be overlapped while maintaining acceptable visibility.

In other words, the extra difficulty in this experiment relies on overlapping the SPDC emission (the crystal plane) in 4 different planes when one of the arms is rotated: the BS plane, the SLM plane, the SMF plane, and a far-field plane on the iCCD sensor.

In the next chapter, we show the results obtained from the implementation of the experimental methods described in this section.

Chapter 3

Results and Analysis

3.1 Hong-Ou-Mandel Interferometer

Figure 3.1 shows an example of the two HOM dips obtained after performing the process embodied in Section 2.1. An experimental data fit was added to each HOM interference pattern as a guide to the eye. In each sub-figure, the average of coincidence counts is different, being around 130 and 6000 for 3.1a and 3.1b respectively. This great difference is explained only by the implementation of the alignment method mentioned in Section 2.4.

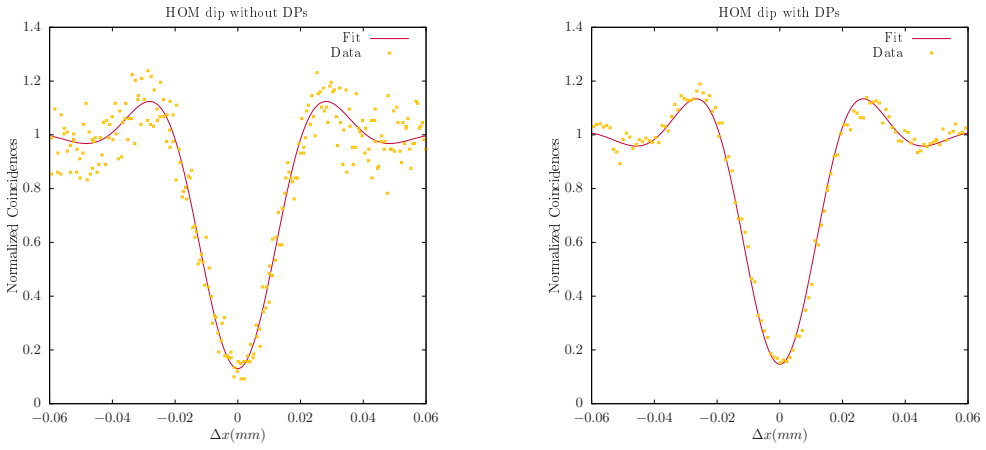

(A) (B)

FIGURE 3.1: HOM experimental dips. Yellow points denote the experimental results, while the red line is a fit made from the experimental data using a Gaussian function multiplied by a Sinc. Results obtained (a) without DPs (b) with DPs.

Since the photons follow a Poisson distribution, the higher the count rate, the smaller the error in the measurement. This is the reason why the first plot seems to have a greater dispersion of the experimental data concerning to the fit. Both measurements were made with an integrating time of $1s$, with steps of $1\mu\ m$ in the motor.

These results show that adding the DPs does not affect substantially the width of the HOM dip, although it was found that reaching high visibility is not as easy as it is when there are not DPs.

3.2 OAM Modes Visualization

Following the method explained in section 2.2, coincidence images were taken for 4 different values of ℓ_s on the OAM-projector. Since the iCCD records on each pixel the number of coincidences, we do not only get the intensity profile in which the idler photon is projected, but also a total number of coincidences when summing all over the image. This feature will be important to obtain the HOM interferometer from the images obtained through the procedure described in 2.3.

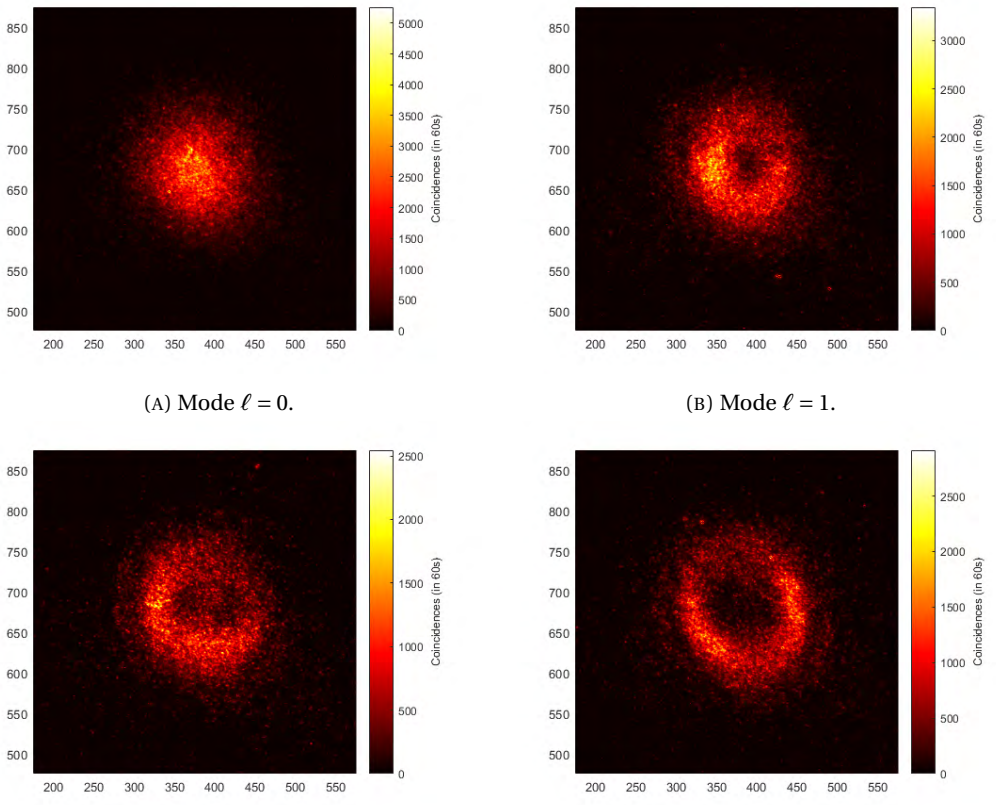

(A) Mode $\ell = 0$.

(B) Mode $\ell = 1$.

(C) Mode $\ell = 2$.

(D) Mode $\ell = 3$.

FIGURE 3.2: Spatial modes of the idler photon when captured in coincidence by the iCCD after the projection of the signal photon on the specified ℓ index.

The images shown in Figure 3.2 exhibit the intensity patterns obtained after a 60s integration. Background subtraction was performed on each image and a noise filter was applied to eliminate high-valued fluctuations. The coincidence counts decrease as long as ℓ is incremented, this is due to the different values of the probability amplitude coefficients $C_{\ell,-\ell}$ from equation (1.24). Since it is not the purpose of this work to reconstruct the produced state, no further confirmation of the ℓ index measured was made apart from the increment of the ring radius size. This experimental implementation was made to confirm the OAM conservation in the non-collinear regimen, so that procedure 2.3 could be implemented.

3.3 Interference Visualization

The set of 355 images, acquired by the procedure explained in Section 2.3, were analyzed to recover the corresponding HOM dip/peak. Consequently, the visibility obtained for each index ℓ studied is reported.

3.3.1 Symmetric Behavior

The mode $LG0$ can be chosen as the first symmetric state since its OAM index is not affected by the DPs, then no relative phase between the photons is expected. This is proved by the image sequence in Figure 3.3, where the coincidence counts decrease as the motor reaches the $\Delta x = 0\ \mu m$ position. A closer look at this sequence of images reveals that the spot does not turn off all at the same time but, instead, it is turning off in an upside-down way. This is an effect of the apparition of an interference fringe due to an imperfect alignment.

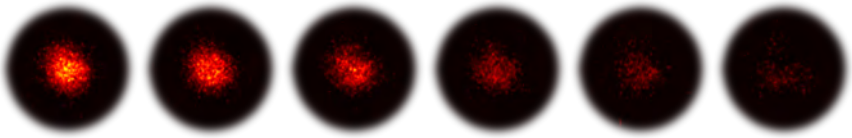

FIGURE 3.3: From left to right, the photo sequence of the $LG0$ mode entering into the HOM dip. The first photo is $\Delta x = -20\ \mu m$ away from maximum interference while the last one corresponds to $\Delta x = 0\ \mu m$.

This last point allows us to claim that the HOM interference contains a spatial structure as a more formal HOM theoretical calculation should show. In a sense, this fringed appearance was to be expected due to the wave description of the photons. An even more important claim should be that photon bunching has a spatial dependency inherited directly, in this case, from the alignment.

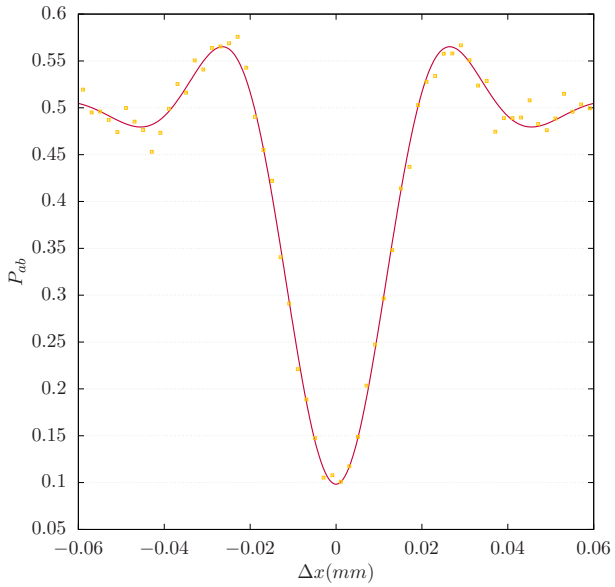

FIGURE 3.4: Hong-Ou-Mandel dip obtained by integrating the experimental images for the mode with $\ell = 0$.

After analyzing the images (see Appendix B), we recover the HOM interference directly from the pictures. The obtained HOM dip is shown in Figure 3.4, where experimental data is represented by yellow squares while the red line is a fit made from the experimental data using a Gaussian function multiplied by a Sinc. By using expression 1.31, the visibility reported is −80.9%, with an estimated uncertainty of ±3% due to its dependence on the parameters used to process the images.

3.3.2 Anti-Symmetric Behavior

The index $\ell = 1$ produces the first anti-symmetric state and then, a peak in the HOM interferometer is expected. This means that as the motor moves to $\Delta x = 0\ \mu m$, the coincidence counts (and then, the mode) must increase its intensity due to photon anti-bunching. This is proved by the image sequence in Figure 3.5.

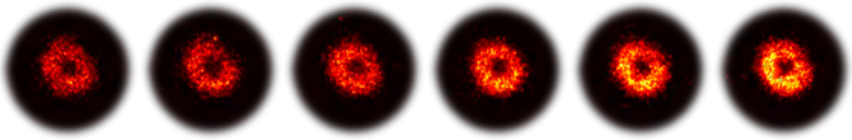

FIGURE 3.5: From left to right, the photo sequence of the $LG1$ mode entering into the HOM peak. The first photo is $\Delta x = -20\ \mu m$ away from maximum interference while the last one corresponds to $\Delta x = 0\ \mu m$.

Despite the increasing number of counts as the interference turns on, the mode does not change its original shape, instead, it becomes brighter as expected. This observation allows us to affirm that HOM interference does not affect mode parameters, such as the beam waist w_0, but only the superposition coefficients. In this particular case, it is not possible to appreciate any interference fringe despite all measurements were done consecutively.

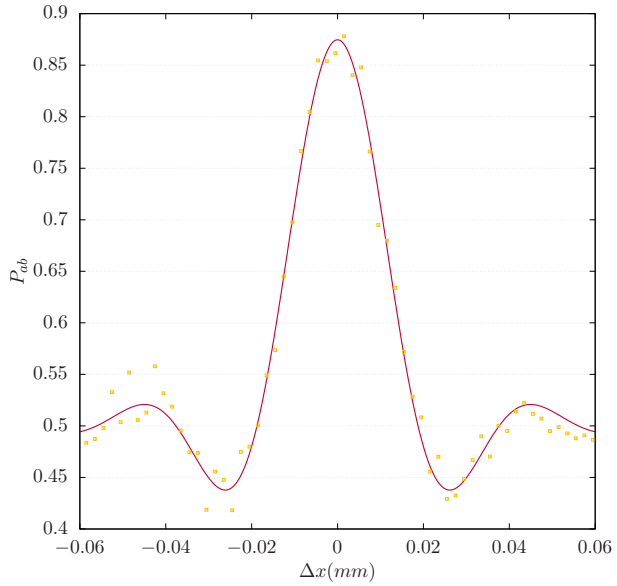

FIGURE 3.6: Hong-Ou-Mandel peak obtained by integrating the experimental images for the anti-symmetric mode corresponding to $\ell = 1$.

The HOM interferogram obtained after analyzing the series of 71 images is shown in Figure 3.6. These data clearly show an anti-bunching behavior as the interference becomes stronger, increasing the coincidence probability. This is proof that the measured state contains a significant anti-symmetric contribution. As we will discuss below, it is not easy to ensure that the engineered state is completely anti-symmetric due to the experimental error introduced when measuring the angle between the DPs.

3.3.3 Interference for Higher Orders

The same procedure as before was repeated for modes $\ell = 2,3$, and 4. An unexpected (but not surprising) result was found. To introduce these results, let us recall Figure 1.2a in which we schematically show how the state symmetry depends on the index ℓ and the angle between the DPs, ϕ.

Consider the case $\phi = 60°$ (red triangles). Depending on each index ℓ, the state symmetry would produce a HOM interference with poor visibility for every state close to the diagonal axes. On the other hand, for $\ell = 3$ it would produce a well visible HOM dip since it lies over the horizontal axis. Tuning the angle between the prisms changes the position of the dots in a continuous way, ranging from the yellow line ($\phi = 60°$) to the brown one ($\phi = 45°$). These small variations of the angle have a direct consequence on the visibility of the corresponding dip/peak, and it becomes more important as the index ℓ becomes greater (see equation (1.32)).

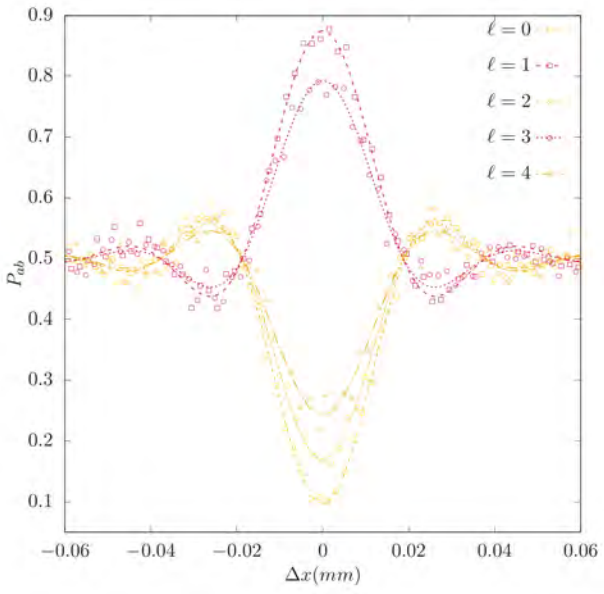

FIGURE 3.7: HOM interferogram for each corresponding index ℓ.

Following these arguments, the visibility obtained varies from the expected as ℓ increases since there is uncertainly in the angle measurement. This can be seen from Figure 3.7, where the different HOM interferograms are shown for indices from $\ell = 0$ to $\ell = 4$. The presence of photon-bunching in the even indices (yellow lines) and anti-bunching in the odd indices (red lines) shows the concept of symmetry-tuning, but it is also possible to see how visibility decrease as the OAM index increase. This meaning that the angle ϕ was not set to exactly 45°, but some value close to it.

A way to find this angle is using equation (1.32), introducing a scaling factor for experimental testing:

$$v = A(2\sin^2\left((2\ell - \ell_p)\phi\right) - 1), \tag{3.1}$$

and performing a fit from the data to find the adjusting parameter ϕ. Doing so, we found the angle between the prism was 47.9°, obtaining the graph shown in Figure 3.8a. The polar representation of the state's symmetry was reproduced for this specific angle and is shown in Figure 3.8b. In congruence with the arguments given earlier, as ℓ becomes greater, the points get more displaced from the horizontal and vertical axes, producing smaller visibility of the HOM dip/peak.

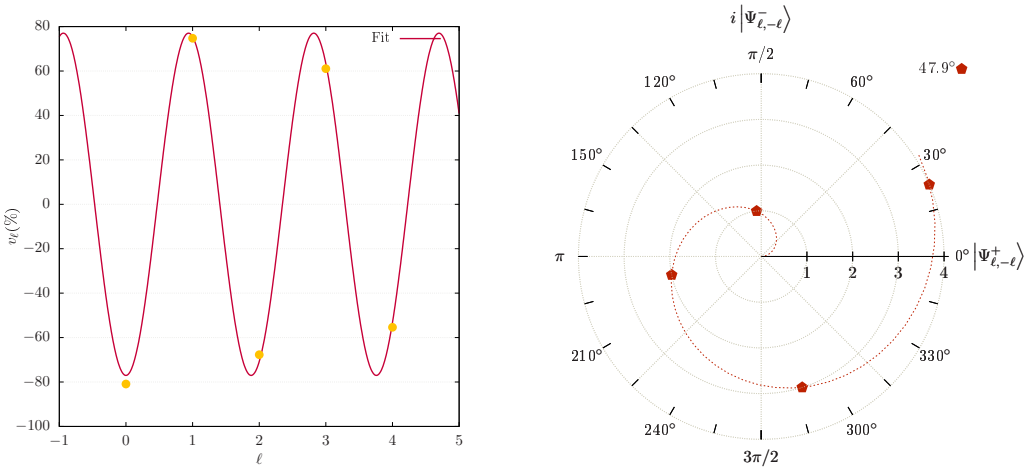

(A) (B)

FIGURE 3.8: (A) Visibility fit from experimental data. (B) Symmetry distribution of the state for the angle obtained through the data fit.

The sequence of the images taken for each of the OAM indices (as those shown in figures 3.3 and 3.5) can be seen scanning the QR code from Figure 3.9.

FIGURE 3.9: Scan the QR code to see the series of images taken or visit https://media.giphy.com/media/bqGp1lt60SksIUCLwv/source.gif.

Chapter 4

Proposed Applications

4.1 Quantum Teleportation

An important application of qubits and their quantum-mechanical properties is known as quantum teleportation (QTP). By means of this technique, Alice can send Bob the information contained in a qubit using a classical channel and a previously shared EPR pair, as presented for the first time by C. Bennet and coworkers in 1993 (*13*). The procedure is relatively simple and is explained below.

As it was mentioned before, Alice and Bob share an EPR pair in any of the Bell's states given in equation (1.20), for example $|\Psi^-\rangle_{AB}$. Suppose Alice wants to send the information of a third qubit, given by Charlie $|\varphi\rangle_C$, to Bob. The joint state of the system may be written as the product state:

$$\begin{aligned} |\Psi\rangle &= |\varphi\rangle_C |\Psi^-\rangle_{AB} \\ &= (\alpha|0\rangle_C + \beta|1\rangle_C)\frac{1}{\sqrt{2}}(|01\rangle_{AB} - |10\rangle_{AB}) \\ &= \frac{1}{\sqrt{2}}\left[\alpha(|001\rangle_{CAB} - |010\rangle_{CAB}) + \beta(|101\rangle_{CAB} - |110\rangle_{CAB})\right] \end{aligned} \tag{4.1}$$

where the notation $|\rangle_C|\rangle_{AB}$ has been reduced to $|\rangle_{CAB}$. Realize that the full computational basis is present between qubits C and A, both belonging to Alice, which leads to the idea of transformation from computational basis to Bell basis following equations (1.21):

$$\begin{aligned} |\Psi\rangle = \frac{1}{2}\big[&|\Phi^+\rangle_{CA}(\alpha|1\rangle_B - \beta|0\rangle_B) + |\Phi^-\rangle_{CA}(\alpha|1\rangle_B + \beta|0\rangle_B) \\ &- |\Psi^+\rangle_{CA}(\alpha|0\rangle_B - \beta|1\rangle_B) - |\Psi^-\rangle_{CA}(\alpha|0\rangle_B + \beta|1\rangle_B)\big]. \end{aligned} \tag{4.2}$$

Several conclusions can be made from this result. First of all, there are four possible outcomes from measuring this state on the Bell basis, all of them with the same probability. Depending of the result of the measurement, Alice will know in which of the superposition states is Bob's qubit. Even though Bob already has his qubit in a superposition given by coefficients α and β after Alice's measurement, the task is not complete until he gets the original state $|\varphi\rangle_C$. Therefore, Alice must communicate Bob the outcome of her measurement, so that he can perform the adequate unitary transformations over his qubit to get the desired result. This can be done by establishing a correspondence rule between the measured Bell state and a pair of classical bits as in Eq. (1.22), or encoding in the first bit whether the coefficients are swapped (01), in the second if they have an additional phase between them (10), or both (11).

There is an important additional aspect of the result (4.2). The initial state shared between Alice and Bob is also the outcome for which no extra operation is needed for Bob to recover $|\varphi\rangle_C$. This comes into play at the moment in which the measurement has to be performed since $|\Psi^-\rangle_{AB}$ is the only anti-symmetric state of the Bell basis and then, the only one leading to coincidence detection after the HOM filter.

After the anti-symmetric state is prepared, the joint state looks similar to equation (4.2) written in the corresponding OAM basis:

$$\begin{aligned}|\Psi\rangle_{CAB} &= \left(\alpha|m\rangle_C + \beta|n\rangle_C\right)\frac{|mn\rangle_{AB} - |nm\rangle_{AB}}{\sqrt{2}} \\ &= \frac{1}{2}\Big[|\Phi^+_{m,n}\rangle_{CA}\left(\alpha|n\rangle_B - \beta|m\rangle_B\right) + |\Phi^-_{m,n}\rangle_{CA}\left(\alpha|n\rangle_B + \beta|m\rangle_B\right) \\ &- |\Psi^+_{m,n}\rangle_{CA}\left(\alpha|m\rangle_B - \beta|n\rangle_B\right) - |\Psi^-_{m,n}\rangle_{CA}\left(\alpha|m\rangle_B + \beta|n\rangle_B\right)\Big],\end{aligned}$$

where, once more, is important to point out that if the anti-symmetric state is detected between photons A and C, no additional operation is needed over B to recover the original state.

Hong-Ou Mandel interference can be used to measure the anti-symmetric contribution between A and C of the state $|\Psi\rangle_{CAB}$ when conditioned to coincidences. This assseveration must be made with extreme care because beam-splitter transformations produce additional terms since there is a three-particle state.

Consider the original joint state in terms of the corresponding operators:

$$|\Psi\rangle_{CAB} \quad = \quad \frac{1}{\sqrt{2}}(\alpha\hat{c}^\dagger_m + \beta\hat{c}^\dagger_n)(\hat{a}^\dagger_m\hat{b}^\dagger_n - \hat{a}^\dagger_n\hat{b}^\dagger_m)|0\rangle_{CAB}.$$

Since the HOM filter acts as a usual HOM interferometer, well-known BS transformations can be applied:

$$\hat{a}^\dagger_i \to \frac{1}{\sqrt{2}}(\hat{a}_i{}^\dagger - \hat{c}_i{}^\dagger) \quad \text{and} \quad \hat{c}^\dagger_i \to \frac{1}{\sqrt{2}}(\hat{a}_i{}^\dagger + \hat{c}_i{}^\dagger).$$

By developing the product, the final state is:

$$\begin{aligned}|\Psi\rangle_{CAB} &= \frac{1}{2\sqrt{2}}\Big(\alpha(\hat{c}^\dagger_m + \hat{a}^\dagger_m) + \beta(\hat{c}^\dagger_n + \hat{a}^\dagger_n)(\hat{a}^\dagger_m - \hat{c}^\dagger_m)\hat{b}^\dagger_n - (\hat{a}^\dagger_n - \hat{c}^\dagger_n)\hat{b}^\dagger_m\Big)|0\rangle_{CAB} \\ &= \frac{1}{2\sqrt{2}}\Big(-\alpha\hat{a}^{\dagger 2}_m\hat{b}^\dagger_n + \alpha\hat{a}^\dagger_n\hat{a}^\dagger_m\hat{b}^\dagger_m - \hat{a}^\dagger_n\hat{a}^\dagger_m\beta\hat{b}^\dagger_n + \hat{a}^{\dagger 2}_n\beta\hat{b}^\dagger_m \\ &\quad -\alpha\hat{a}^\dagger_m\hat{b}^\dagger_m\hat{c}^\dagger_n + \alpha\hat{a}^\dagger_n\hat{b}^\dagger_m\hat{c}^\dagger_m - \hat{a}^\dagger_m\beta\hat{b}^\dagger_n\hat{c}^\dagger_n + \hat{a}^\dagger_n\beta\hat{b}^\dagger_n\hat{c}^\dagger_m \\ &\quad +\alpha\hat{b}^\dagger_n\hat{c}^{\dagger 2}_m - \alpha\hat{b}^\dagger_m\hat{c}^\dagger_m\hat{c}^\dagger_n - \beta\hat{b}^\dagger_m\hat{c}^{\dagger 2}_n + \beta\hat{b}^\dagger_n\hat{c}^\dagger_m\hat{c}^\dagger_n\Big)|0\rangle_{CAB}.\end{aligned}$$

This twelve-terms result seems to have no further conclusion about the state to be measured, but if only terms involving one photon in each path are considered (coincidence detection between A,B, and C), the expression is reduced to just four terms:

$$\begin{aligned}|\Psi\rangle_{CAB} &= \kappa\Big(\hat{c}^\dagger_m\hat{a}^\dagger_n(\alpha\hat{b}^\dagger_m + \beta\hat{b}^\dagger_n) - \hat{c}^\dagger_n\hat{a}^\dagger_m(\alpha\hat{b}^\dagger_m + \beta\hat{b}^\dagger_n)\Big)|0\rangle_{CAB} \\ |\Psi\rangle_{CAB} &= \kappa|\Psi^-_{m,n}\rangle_{CA}\left(\alpha|m\rangle_B + \beta|n\rangle_B\right).\end{aligned}$$

The normalization constant κ is added due to the elimination of the non-coincidence terms. To summarize, if photons A and C are introduced in a HOM interferometer, only

the anti-symmetric contribution of the whole state will lead to coincidence measurements.

By inspection of the previous result, is clear to see that the resulting state on photon B is the initial state of photon C.

There is an important difference between the procedure shown here and that leading to eq. (4.2): m and n are any pair of indices satisfying $\left|\Psi^{-}_{m,n}\right\rangle_{AB}$ as the input state of photons A and B.

A naive proposal for an experimental setup to implement the protocol described before is shown in Figure 4.1. It consists of a source of entangled pairs engineered into the $\left|\Psi^{-}_{m,n}\right\rangle_{AB}$ state through the DPs. A third photon created by a secondary SPDC emission is projected into the desired $\left|\varphi\right\rangle_{C}$ state by means of an SLM. Photon D is unmeasured. A member of the entangled pair AB is introduced into the anti-symmetric filter along with the photon C, such that they are projected by an SLM on the SMFs. If the iCCD camera is triggered by coincidence counts, then the $\left|\varphi\right\rangle_{C}$ state should be visible.

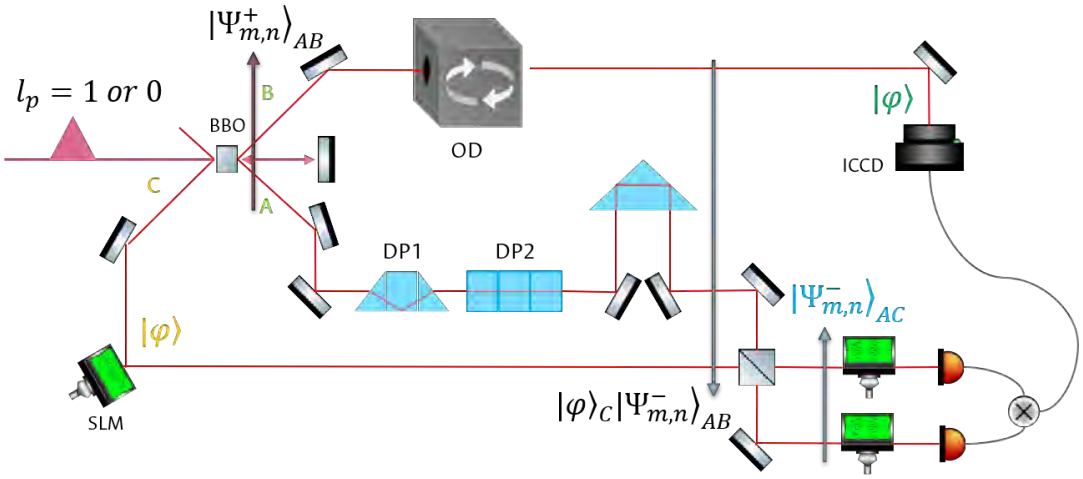

FIGURE 4.1: Experimental proposal for Quantum Teleportation implementation in the OAM degree of freedom. OD: optical delay.

The experimental proposal includes the possibility of pumping with different OAM indices ℓ_p since, as equation 1.26 shows, it is possible to engineer all pairs to be in an anti-symmetric state by using $\ell_p = 1$.

4.2 Quantum Imaging

Ghost Imaging (GI) is a technique that exploits the quantum correlations, in position and momentum, of quantum systems to reconstruct the image of an object (*48*). The idea is to exploit these correlations to recreate the image of the object using light that has not interacted with it, hence the name.

These spatial correlations allow reconstructing the image of the aperture disposed on the signal photon by scanning the idler, searching for coincidence counts. Since then, there have been done many studies for reducing the time required for the acquisition of such

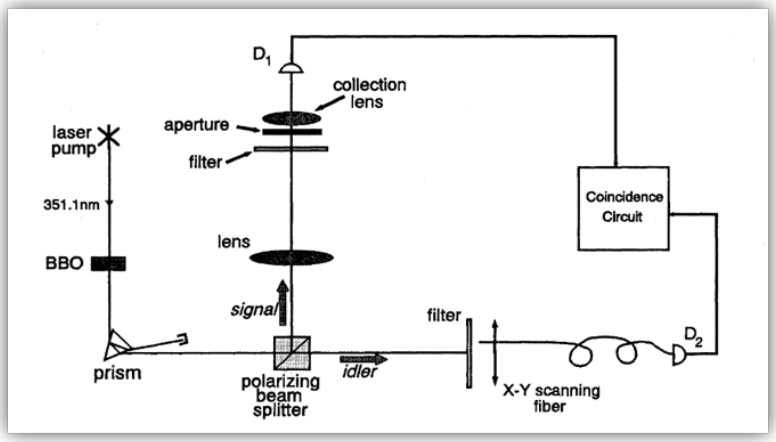

FIGURE 4.2: Original set-up for implementation of GI. Taken from (*48*).

images, as well as enhance their quality (*28*, *49*, *50*). Most of these techniques are designed to improve GI made using bucket detectors, but, as we count with an iCCD camera, spatially resolved measurements are relatively direct to obtain.

Implementation of GI using OAM-entangled symmetric and anti-symmetric states has already been done by Bornman *et al.* (*29*) using the same experimental set-up implemented by Y. Zhang *et al.* to produce and filter this kind of state. It was shown that the image obtained was a double ghost image given by the superposition of reflected and transmitted light with a relative rotation due to the angle between the DPs. Nonetheless their work, there is no exploration of the superposition of symmetric and anti-symmetric states, for which different results could be achieved.

Since we are able to spatially resolve the symmetry of the state in terms of its HOM interference, it should be possible to engineer a phase mask such that it projects a different OAM state (symmetric or anti-symmetric) depending on each image region. This phase mask must have a given symmetry due to the rotated superposition of the modes.

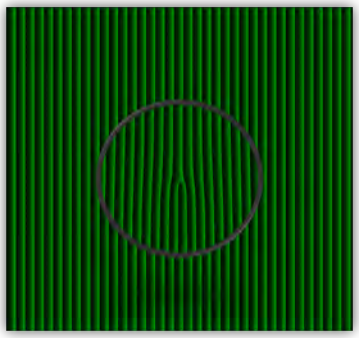

FIGURE 4.3: Phase mask proposed as a simple proof-of-concept to implement spatially resolved measurement of the symmetry of the state.

Figure 4.3 shows an example of a phase mask to test the idea as proof-of-concept. The region within the circle contains the phase mask used to project the photon into the $\ell = 1$ mode, while the external square is made by the $\ell = 0$ mask (without singularity). As the interference becomes more important, the inner circle should increase its intensity while the external region darkens, giving place to a double-contrast to define the circle. On top

of that, we would be performing a spatially resolved measurement of the symmetry of the state.

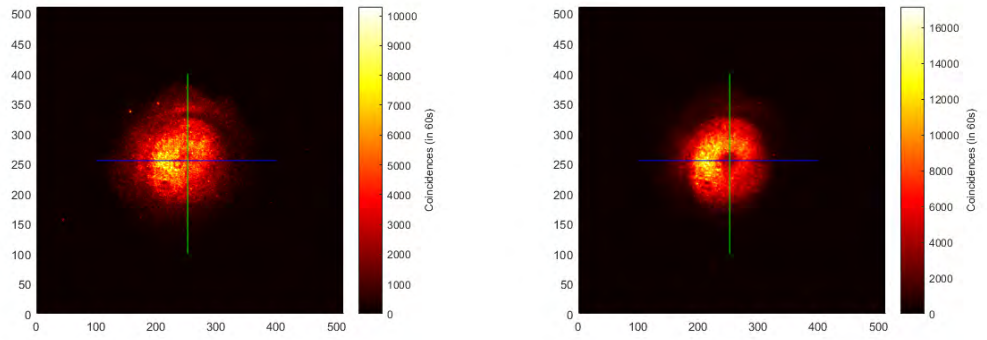

(A) $\Delta x \sim \infty$ (B) $\Delta x = 0$

FIGURE 4.4: Ghost Imaging of the phase mask displayed on the SLM (A) Far from maximum interference. (B) With maximum interference.

Using the phase mask shown in Figure 4.3, we got the images inside and far away from the maximum interference. Figure 4.4 shows these two acquisitions in which differences are observed in the sharpness with which the circle is defined and the singularity in its interior. The inner area of the image is illuminated by an LG mode with $\ell = 1$ while the outer area corresponds to a Gaussian mode, as Figure 4.4a shows. Once the interference plays its role, the circle will increase its brightness (counts) while the zone around it darkens producing better image contrast and definition.

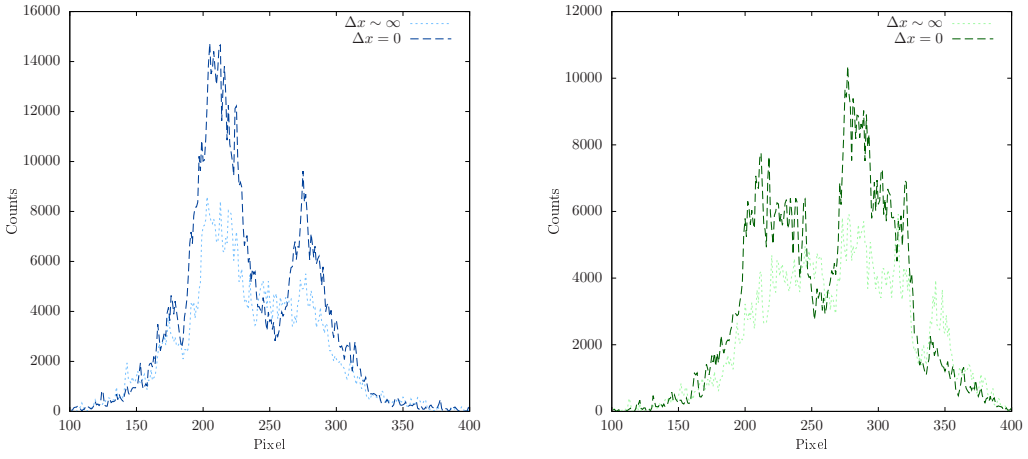

(A) (B)

FIGURE 4.5: Intensity profiles of images taken. Light colors correspond to the photo far from the interference, while strong colors correspond to the maximally interfered image. (A) Horizontal profile (B) Vertical profile.

As the anti-symmetric part of the image increase its counts while the symmetric part decreases them, the product is a better definition of the image edges. Figure 4.5 shows the different profiles extracted from the images shown in Figure 4.4. The blue lines correspond to the horizontal profile while the green lines to the vertical ones.

Chapter 5

Conclusions and Future Work

We implemented a spatially resolved version of Zhang's experiment (*26*) using an iCCD camera along with an optical delay. Beyond that, we performed a study of how these engineered states are produced in terms of the pumping index ℓ_p and showed that the visibility can be used as a measurement of the symmetric or anti-symmetric contribution of the state. We proposed a way to visualize these two contributions using the polar plots shown in Figure 1.2.

Furthermore, we recovered the HOM interferometer from the pictures taken after building our setup. The experimental difficulty of this experiment led us to propose an ingenious form of alignment that proved to be highly accurate.

This study also showed that HOM interference has a spatial structure that has to be reviewed theoretically in the way to purpose new applications. One of these studies should be the theoretical development of the double contrast ghost imaging we implemented experimentally. On the other hand, we included quantum teleportation as a new application for these engineered states and we proposed a possible way to do it experimentally.

Appendix A

Pump characterization

To characterize the pump beam size, 20 pictures were taken in positions 2.5 cm apart from each other such that the beam waist was in that range. For each picture, a circle that enclosed the %97.6 (first Airy radius) of the intensity was found. With these data, a fit with the form:

$$w(x) = w_0\sqrt{1+\left(\frac{x-L}{z}\right)^2}$$

was performed through Gnuplot to find the fit parameter w_0 (see Figure A.1).

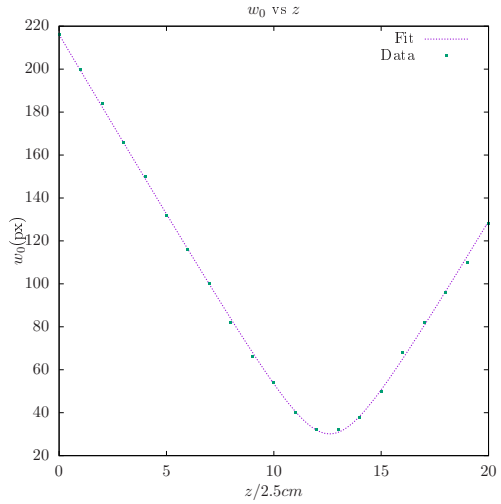

FIGURE A.1: Dots correspond to beam radius. The dashed line shows the fit to the previous equation.

The beam waist is obtained by the product of the w_0 obtained from the fit and the pixel size.

Appendix B

Image Processing

An example of a raw image acquired for the *LG*0 mode by the iCCD can be seen in Figure B.1a. This picture is made by the number of counts accumulated by the iCCD on each pixel. Despite the conditioning triggering of the camera, there are around 800 counts per pixel coming from accidental counts, fluctuations, among others. On top of that, some points in the image contain high-valued fluctuations that must be removed.

In order to do that, a noise filter was applied to the raw image by finding pixels with values higher than 1.5 times the mean of a neighborhood defined by a circle of 2 pixels of radius. The resulting image is shown in Figure B.1b. Some of the most noticeable effects of this filter can be seen by inspecting two regions. The first one is around coordinates $(110, 45)$, where a high-valued pixel far from the gaussian spot has been removed. The second region is the fluctuation near to $(125, 65)$, where the high-valued spot has been attenuated.

Since the noise filter does not remove the background counts, it is necessary to define a threshold to distinguish the desired signal from the noise. To do so, we found a circular region, centered on the mode, that enclosed 35% of the total counts. The average of the pixels out of that region was computed and subtracted to the signal, negative values were taken as zero. Figures B.1c and B.1d show the region enclosed by the circle and the background-subtracted image respectively. Notice that maximum counts still in the same order as before the background subtraction.

Finally, we defined a region of interest such that it enclosed 85% of the total counts but in the corresponding dip/peak image. We ensured that this region was large enough for each studied mode. An example is shown in Figure B.1e. To find the number of coincidences, we integrate the same region on each image for each corresponding series of 71 images.

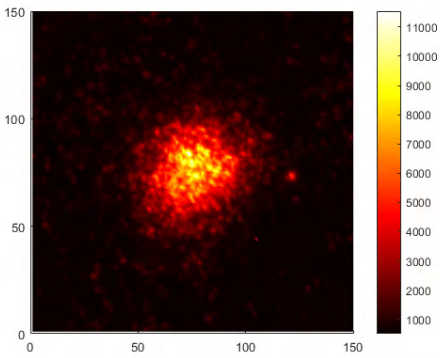

(A) Raw data.

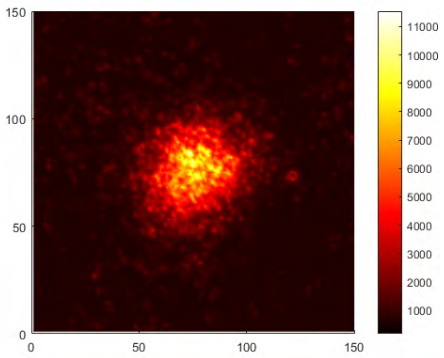

(B) Image after the conditional noise filter.

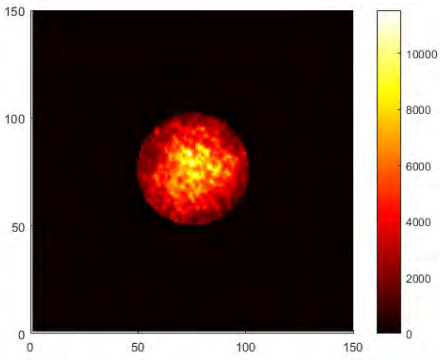

(C) Zone from which background threshold is obtained.

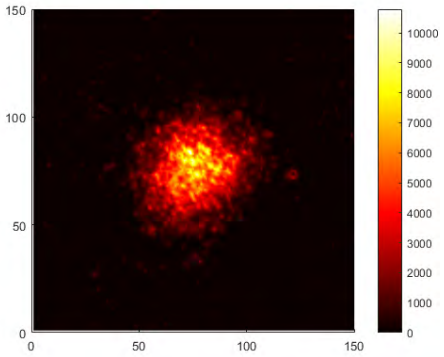

(D) Image after background subtraction.

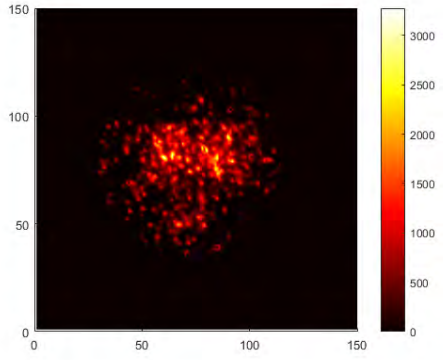

(E) The Region of interest is defined by the mode intensity on the corresponding dip/peak.

Bibliography

1. A. Einstein, B. Podolsky, N. Rosen, en, *Physical Review* **47**, 777–780, ISSN: 0031-899X, (2020; https://link.aps.org/doi/10.1103/PhysRev.47.777) (May 1935).
2. J. S. Bell, en, *Physics Physique Fizika* **1**, 195–200, ISSN: 0554-128X, (2020; https://link.aps.org/doi/10.1103/PhysicsPhysiqueFizika.1.195) (Nov. 1964).
3. S. P. Gudder, en, *Journal of Mathematical Physics* **11**, 431–436, ISSN: 0022-2488, 1089-7658, (2021; http://aip.scitation.org/doi/10.1063/1.1665156) (Feb. 1970).
4. A. Aspect, en, *Physical Review D* **14**, 1944–1951, ISSN: 0556-2821, (2020; https://link.aps.org/doi/10.1103/PhysRevD.14.1944) (Oct. 1976).
5. A. Aspect, P. Grangier, G. Roger, en, *Physical Review Letters* **49**, 91–94, ISSN: 0031-9007, (2021; https://link.aps.org/doi/10.1103/PhysRevLett.49.91) (July 1982).
6. B. Hensen *et al.*, en, *Nature* **526**, 682–686, ISSN: 0028-0836, 1476-4687, (2021; http://www.nature.com/articles/nature15759) (Oct. 2015).
7. M. Giustina *et al.*, en, *Physical Review Letters* **115**, 250401, ISSN: 0031-9007, 1079-7114, (2021; https://link.aps.org/doi/10.1103/PhysRevLett.115.250401) (Dec. 2015).
8. L. K. Shalm *et al.*, en, *Physical Review Letters* **115**, 250402, ISSN: 0031-9007, 1079-7114, (2021; https://link.aps.org/doi/10.1103/PhysRevLett.115.250402) (Dec. 2015).
9. W. P. Schleich *et al.*, en, *Applied Physics B* **122**, 130, ISSN: 0946-2171, 1432-0649, (2020; http://link.springer.com/10.1007/s00340-016-6353-8) (May 2016).
10. H. Bachor, T. C. Ralph, *A Guide to Experiments in Quantum Optics*, en (Wiley, ed. 1, Sept. 2019), ISBN: 978-3-527-41193-1 978-3-527-69580-5, (2021; https://onlinelibrary.wiley.com/doi/book/10.1002/9783527695805).
11. I. A. Walmsley, en, *Science* **348**, 525–530, ISSN: 0036-8075, 1095-9203, (2021; https://www.sciencemag.org/lookup/doi/10.1126/science.aab0097) (May 2015).
12. D. Browne, S. Bose, F. Mintert, M. Kim, en, *Progress in Quantum Electronics* **54**, 2–18, ISSN: 00796727, (2021; https://linkinghub.elsevier.com/retrieve/pii/S0079672717300186) (Aug. 2017).
13. C. H. Bennett *et al.*, en, *Physical Review Letters* **70**, 1895–1899, ISSN: 0031-9007, (2020; https://link.aps.org/doi/10.1103/PhysRevLett.70.1895) (Mar. 1993).
14. J.-W. Pan, D. Bouwmeester, H. Weinfurter, A. Zeilinger, en, *Physical Review Letters* **80**, 3891–3894, ISSN: 0031-9007, 1079-7114, (2021; https://link.aps.org/doi/10.1103/PhysRevLett.80.3891) (May 1998).
15. C. H. Bennett, G. Brassard, en, *Theoretical Computer Science* **560**, 7–11, ISSN: 03043975, (2020; https://linkinghub.elsevier.com/retrieve/pii/S0304397514004241) (Dec. 2014).
16. C. H. Bennett, S. J. Wiesner, en, *Physical Review Letters* **69**, 2881–2884, ISSN: 0031-9007, (2020; https://link.aps.org/doi/10.1103/PhysRevLett.69.2881) (Nov. 1992).

17. A. Zeilinger, G. Weihs, T. Jennewein, M. Aspelmeyer, en, *Nature* **433**, 230–238, ISSN: 0028-0836, 1476-4687, (2020; http://www.nature.com/articles/nature03280) (Jan. 2005).
18. L. Allen, M. W. Beijersbergen, R. J. C. Spreeuw, J. P. Woerdman, en, *Physical Review A* **45**, 8185–8189, ISSN: 1050-2947, 1094-1622, (2020; https://link.aps.org/doi/10.1103/PhysRevA.45.8185) (June 1992).
19. D. L. Andrews, M. Babiker, Eds., *The angular momentum of light* (Cambridge University Press, Cambridge, UK, 2013), ISBN: 978-1-107-00634-8.
20. M. Erhard, R. Fickler, M. Krenn, A. Zeilinger, en, *Light: Science & Applications* **7**, 17146–17146, ISSN: 2047-7538, (2020; http://www.nature.com/articles/lsa2017146) (Mar. 2018).
21. M. Krenn, M. Malik, M. Erhard, A. Zeilinger, en, *Philosophical Transactions of the Royal Society A: Mathematical, Physical and Engineering Sciences* **375**, 20150442, ISSN: 1364-503X, 1471-2962, (2021; https://royalsocietypublishing.org/doi/10.1098/rsta.2015.0442) (Feb. 2017).
22. M. Mirhosseini *et al.*, *New Journal of Physics* **17**, 033033, ISSN: 1367-2630, (2021; https://iopscience.iop.org/article/10.1088/1367-2630/17/3/033033) (Mar. 2015).
23. J. Romero, D. Giovannini, S. Franke-Arnold, S. M. Barnett, M. J. Padgett, presented at the, ed. by G. W. Kamerman *et al.*, 85421S, (2021; http://proceedings.spiedigitallibrary.org/proceeding.aspx?doi=10.1117/12.979888).
24. D.-S. Ding *et al.*, en, *Communications Physics* **2**, 100, ISSN: 2399-3650, (2021; http://www.nature.com/articles/s42005-019-0201-1) (Dec. 2019).
25. Y. Zhang *et al.*, en, *Nature Communications* **8**, 632, ISSN: 2041-1723, (2020; http://www.nature.com/articles/s41467-017-00706-1) (Dec. 2017).
26. Y. Zhang *et al.*, en, *Science Advances* **2**, e1501165, ISSN: 2375-2548, (2020; https://advances.sciencemag.org/lookup/doi/10.1126/sciadv.1501165) (Feb. 2016).
27. A. Babazadeh *et al.*, en, *Physical Review Letters* **119**, 180510, ISSN: 0031-9007, 1079-7114, (2021; https://link.aps.org/doi/10.1103/PhysRevLett.119.180510) (Nov. 2017).
28. X. Gao, M. Erhard, A. Zeilinger, M. Krenn, en, *Physical Review Letters* **125**, 050501, ISSN: 0031-9007, 1079-7114, (2021; https://link.aps.org/doi/10.1103/PhysRevLett.125.050501) (July 2020).
29. N. Bornman, S. Prabhakar, A. Vallés, J. Leach, A. Forbes, *New Journal of Physics* **21**, 073044, ISSN: 1367-2630, (2021; https://iopscience.iop.org/article/10.1088/1367-2630/ab2f4d) (July 2019).
30. P. Yepiz-Graciano, A. M. A. Martínez, D. Lopez-Mago, H. Cruz-Ramirez, A. B. U'Ren, en, *Photonics Research* **8**, 1023, ISSN: 2327-9125, (2021; https://www.osapublishing.org/abstract.cfm?URI=prj-8-6-1023) (June 2020).
31. F. Bouchard *et al.*, *Reports on Progress in Physics* **84**, arXiv: 2006.09335, 012402, ISSN: 0034-4885, 1361-6633, (2021; http://arxiv.org/abs/2006.09335) (Jan. 2021).
32. D. L. Andrews, Ed., *Structured light and its applications: an introduction to phase-structured beams and nanoscale optical forces*, OCLC: ocn191244950 (Academic, Amsterdam ; Boston, 2008), ISBN: 978-0-12-374027-4.
33. Y. Zhang *et al.*, en, *Physical Review A* **94**, 033855, ISSN: 2469-9926, 2469-9934, (2021; https://link.aps.org/doi/10.1103/PhysRevA.94.033855) (Sept. 2016).
34. A. Crespi *et al.*, en, *Nature Communications* **2**, 566, ISSN: 2041-1723, (2021; http://www.nature.com/articles/ncomms1570) (Sept. 2011).

35. M. Russ, G. Burkard, en, *Journal of Physics: Condensed Matter* **29**, 393001, ISSN: 0953-8984, 1361-648X, (2021; https://iopscience.iop.org/article/10.1088/1361-648X/aa761f) (Oct. 2017).

36. I. I. Beterov, en, *Optoelectronics, Instrumentation and Data Processing* **56**, 317–324, ISSN: 8756-6990, 1934-7944, (2021; http://link.springer.com/10.3103/S8756699020040020) (July 2020).

37. D. Cozzolino, B. Da Lio, D. Bacco, L. K. Oxenløwe, en, *Advanced Quantum Technologies* **2**, 1900038, ISSN: 2511-9044, 2511-9044, (2021; https://onlinelibrary.wiley.com/doi/10.1002/qute.201900038) (Dec. 2019).

38. M. Erhard, M. Krenn, A. Zeilinger, en, *Nature Reviews Physics* **2**, 365–381, ISSN: 2522-5820, (2021; http://www.nature.com/articles/s42254-020-0193-5) (July 2020).

39. A. Mair, A. Vaziri, G. Weihs, A. Zeilinger, en, *Nature* **412**, 313–316, ISSN: 0028-0836, 1476-4687, (2020; http://www.nature.com/articles/35085529) (July 2001).

40. J. P. Torres, A. Alexandrescu, L. Torner, en, *Physical Review A* **68**, 050301, ISSN: 1050-2947, 1094-1622, (2020; https://link.aps.org/doi/10.1103/PhysRevA.68.050301) (Nov. 2003).

41. F. M. Miatto, A. M. Yao, S. M. Barnett, en, *Physical Review A* **83**, 033816, ISSN: 1050-2947, 1094-1622, (2020; https://link.aps.org/doi/10.1103/PhysRevA.83.033816) (Mar. 2011).

42. C. K. Hong, Z. Y. Ou, L. Mandel, en, *Physical Review Letters* **59**, 2044–2046, ISSN: 0031-9007, (2020; https://link.aps.org/doi/10.1103/PhysRevLett.59.2044) (Nov. 1987).

43. A. M. Brańczyk, *arXiv:1711.00080 [quant-ph]*, arXiv: 1711.00080, (2021; http://arxiv.org/abs/1711.00080) (Oct. 2017).

44. M. Fox, *Quantum optics: an introduction* (Oxford University Press, Oxford ; New York, 2006), ISBN: 978-0-19-856672-4 978-0-19-856673-1.

45. Z. Y. Ou, J.-K. Rhee, L. J. Wang, en, *Physical Review A* **60**, 593–604, ISSN: 1050-2947, 1094-1622, (2021; https://link.aps.org/doi/10.1103/PhysRevA.60.593) (July 1999).

46. Z. Ibarra-Borja *et al.*, en, *Optics Express* **27**, 25228, ISSN: 1094-4087, (2021; https://www.osapublishing.org/abstract.cfm?URI=oe-27-18-25228) (Sept. 2019).

47. V. Bazhenov, M. Soskin, M. Vasnetsov, en, *Journal of Modern Optics* **39**, 985–990, ISSN: 0950-0340, 1362-3044, (2021; https://www.tandfonline.com/doi/full/10.1080/09500349214551011) (May 1992).

48. T. B. Pittman, Y. H. Shih, D. V. Strekalov, A. V. Sergienko, en, *Physical Review A* **52**, R3429–R3432, ISSN: 1050-2947, 1094-1622, (2021; https://link.aps.org/doi/10.1103/PhysRevA.52.R3429) (Nov. 1995).

49. O. Katz, Y. Bromberg, Y. Silberberg, en, *Applied Physics Letters* **95**, 131110, ISSN: 0003-6951, 1077-3118, (2021; http://aip.scitation.org/doi/10.1063/1.3238296) (Sept. 2009).

50. S. Karmakar, Y. Shih, en, *Physical Review A* **81**, 033845, ISSN: 1050-2947, 1094-1622, (2021; https://link.aps.org/doi/10.1103/PhysRevA.81.033845) (Mar. 2010).